ISSN Print : 2320-2084, Online : 2321-2950

INTERNATIONAL JOURNAL OF ELECTRICAL, ELECTRONICS AND DATA COMMUNICATION (IJEEDC)

VOLUME NO. 11
ISSUE NO. 1
JANUARY - APRIL 2023

ISSN Print : 2320-2084, Online : 2321-2950

International Journal of Electrical, Electronics and Data Communication (IJEEDC)

Aim & Scope

International Journal of Electrical, Electronics and Data Communication (IJEEDC) is having eISSN: 2320-2084 , pISSN:2321-2950, Peer reviewed, Open Access, Indexed and monthly International Journal, being published since year 2013.

IJEEDC is an academic highly reputed, online, open access, peer reviewed international journal. It aims to publish original, theoretical and practical advances in Computer Electrical, Electronics and Communication Engineering and all interdisciplinary streams of Engineering Sciences. All submitted papers will be reviewed by the board of committee of IJEEDC.

Goals Our goals are to promote the co-operation between the professionals in various fields of the Engineering and management to cultivate an environment for the advance and development of the technology. Our objective includes

- Promoting the interactions between the Electrical, Electronics and Communication Engineering
- Advancing the application of engineering techniques from the academics to the industry.
- Facilitating the exchange of information and ideas among the engineers, Scientists, Researchers and academicians easily.

Original ideas may be discussed in advance with the Editor (mail: info.ijeedc@gmail.com), to clear the ground for a draft submission. All papers are then peer-reviewed by relevant experts and feedback is given whether or not a paper is accepted or returned for further work. The Editor's policy is to try and accommodate contributions of all sizes above the minimum threshold where length is dictated by the needs of the subject matter.

IJEEDC publishes both theoretical and experimental high-quality papers of permanent interest, In addition to peer-reviewed original research papers, the Editorial Board welcomes original research reports, state-of-the-art reviews and communications in the broadly defined field of Electronics, Electrical Engineering and Data Communication.

The Journal can be found from the official URL www.ijeedc.iraj.in

ISSN Print : 2320-2084, Online : 2321-2950

ISSN Print : 2320-2084, Online : 2321-2950

ISSN Print : 2320-2084, Online : 2321-2950

ISSN Print : 2320-2084, Online : 2321-2950

International Journal of Electrical Electronics and Data Communication (IJEEDC)

(Volume No. 11, Issue No. 1, January - April 2023)

Contents

ISSN Print : 2320-2084, Online : 2321-2950

DESIGN OF DIAGONALLY SLOTTED MICROSTRIP ANTENNA FOR WIRELESS APPLICATIONS

SHIPRA SRIVASTAVA , VIBHAV KUMAR SACHAN , SAPTARSHI GUPTA, SATYA SAI SRIKANT
SRM Institute of Science and Technology, Delhi NCR, Modinagar, India
KIET Group of Institutions, Delhi NCR, Ghaziabad, India

ABSTRACT

It is well known that for every one wavelength and the polarization plane in Antenna and Electromagnetic signal makes one complete circle in a corkscrew pattern. This paper presents about circular polarization of planar antenna, which has been designed with IE3D electromagnetic simulator. Four distinct geometries were designed with two diagonally etched slots for microstrip patch antenna. This paper also demonstrates about the circular polarization with the help of four slots in the form of squares, circles, rings, and crosses were chosen. Also other parameters like Axial Ratio performance plot, Reflection coefficient and Impedance plot were studied. This paper also discuss about one of the above mentioned antenna, which was fabricated and tested properly.

***Keywords-* Diagonally Slotted Patch Antenna, Axial Ratio, VSWR, Circular Polarization, Gain**

I. INTRODUCTION

Now a days, planar antennas are playing important role in digital and wireless communication area. It's because they are not only light and compact but also it is easy to handle, perfectly aerodynamic and more important it has conformal qualities property. Circular polarization, an unavoidable property for antenna design is currently in demand in today's digital communication system. Various researchers and scientists are continuously working with various innovative techniques in antenna and its properties since last three decades [1].

The researchers are also continuously exploring the antenna design using a multi-layered structure with various techniques using coupling gap and probe feeds. Good return loss, a wide bandwidth range and excellent radiation pattern are all few features of such antenna. One of the researchers Ushjima et.al investigated for stacked microstrip antenna to obtain orthogonal dual linear polarization [2]. one of the researcher T Wu and his team, Wu et.al (2013) has investigated and designed switchable broadband stacked microstrip antenna with four-pin diode to achieve circular polarization, which was used for 2.45-GHz RFID reader [3]. Circular and linear polarizations can be achieved and can be interchanged with various designs [4-11].

II. ANTENNA DESIGN

Antenna matching is one of the major improves property when the antenna size is controlled. In this paper, a circularly-polarized array antenna has been designed and simulated with a gain of 4.1 dBi @ 1GHz frequency. Equally-polarized patch was placed linearly equidistant, with perfect matching in order to achieve circular polarization. The structure and basic behaviour of the designed linearly polarized array antenna, as well as its simulation results, are shown in subsequent section. The present paper contains two distinct shaped slots, which were carved diagonally of the microstrip antenna.

Four different slots with varying forms were chosen and designed diagonally for evaluating the circular polarizations with various factors. The various slots are square slots, crossed (plus) slots, concentric ring slots and circular slots, which are shown in Fig 1, Fig 2, Fig 3 and Fig 4 respectively.

All the circularly polarized patch antenna (as shown in all figures) were designed in a single-layer dielectric substrate with epoxy glass having dielectric constant (ἐr) = 4.2 and thickness of 4.4 mm which has an overall loss of 0.025%. A distance of 15-mm is used and designed to feed antenna patches in all the configurations, from the x axis. Table1 shows the common architectural specification of the designed antennas.

Sr No	Parameters	Measurement (mm)
1.	Loss tangent	0.024
2.	Dielectric constant	4.4
3.	Feeding distance	15 mm
4.	Area dimension	100mm X100mm
5.	Dielectric layer height	1.6 mm
6.	Patch dimension	78mm X 78mm

Table 1. Specifications of designed antennas

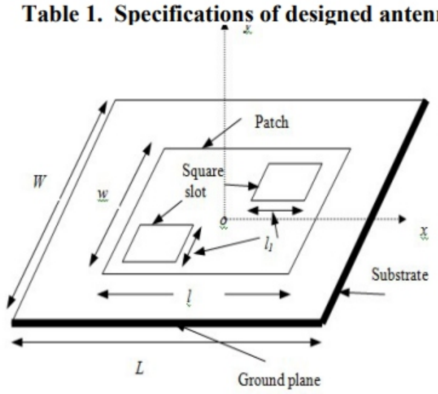

Fig 1 Two Squares slotted diagonally in microstrip patch antenna

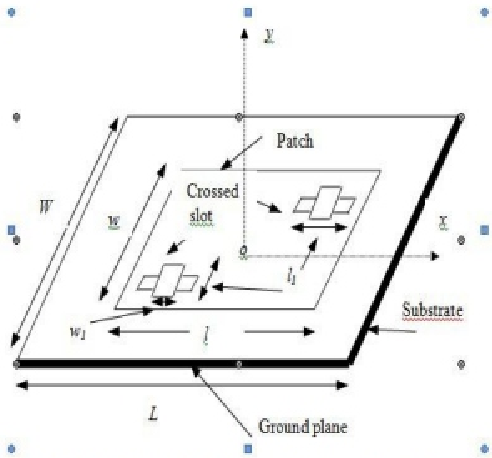

Fig 2. Cross (plus) slotted diagonally in microstrip patch antenna

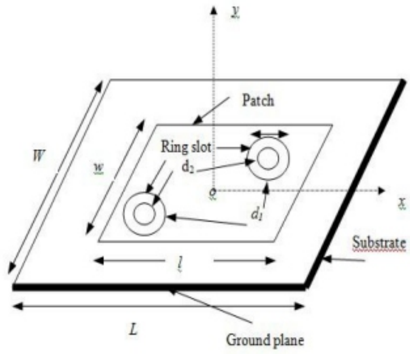

Fig 3. Two Concentric ring, slotted diagonally in microstrip patch antenna

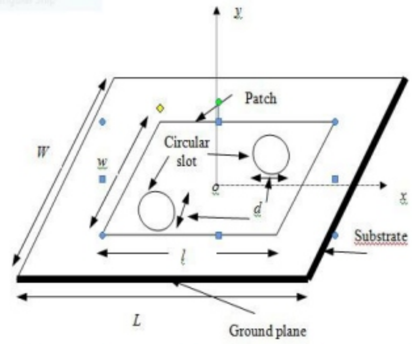

Fig 4 Two circles, slotted diagonally in microstrip patch antenna

A high frequency electromagnetic simulator based on the Method of Moment (IE3D) was selected to design a circularly polarized antenna. The pattern computation and current distribution tabs were activated in the simulation with various parameters as mentioned in Table I mentioned. The architectural parameters of slotted dimensions as specified in Table 2 were slotted in the microstrip antenna. These slotted dimensions were achieved by hit and trial method in order to obtain circular polarization

Parameters	Measurement(mm)
Horizontal Length	21.5
Vertical Length	5
Ring Outer Diameter	7.5
Ring Inner Diameter	6.5
Circular Slot Diameter	7
Square slot	14 X 14

Table 2. Specifications of slotted pattern

III. RESULTS AND DISCUSSIONS

Four different form slots in the square microstrip patch were designed and simulated to investigate their circular polarization in the antennas. It is observed from the simulated results of all the four slotted microstrip antennas from the plots in Figures 5(a)-(d), all four antennas have an axial ratio that is within the required range of 4 dB for a circularly polarized signal. The return loss of Fig 6 is evaluated from I3ED simulator for Antenna 1 (as per Fig 6) in the form of reflection coefficient. Future studies are in process for all the antennas.

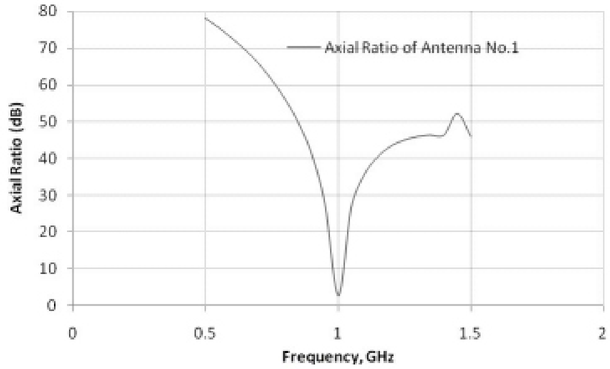

(a)

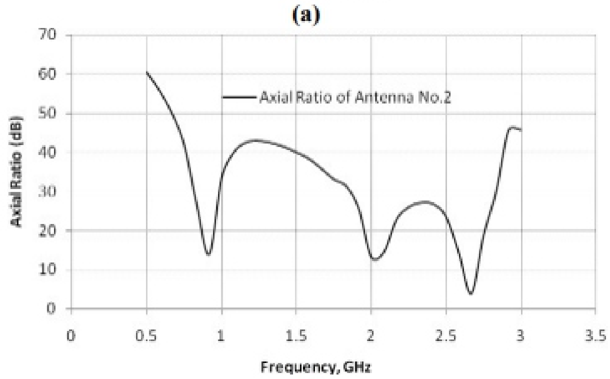

(b)

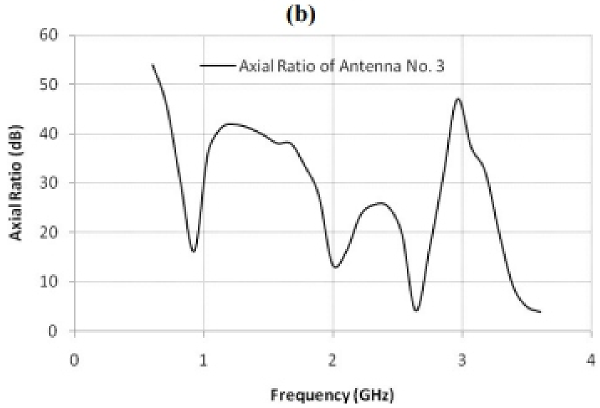

(c)

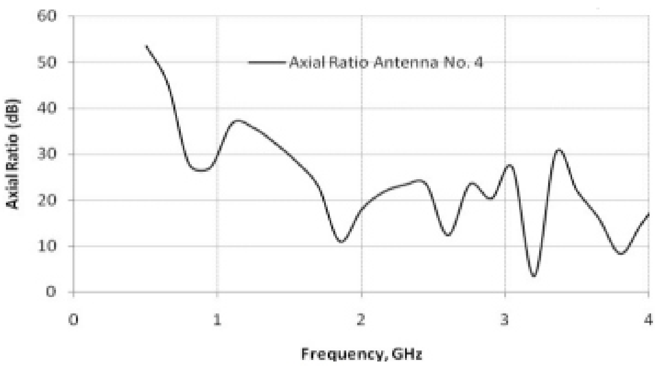

(d)

Fig 5. Antenna 1 to Antenna 4: Axial ratio plot

An antenna was fabricated for two squares diagonallyslotted in microstrip patch antenna as shown in Fig 7 has been fabricated as per material mentioned for Antenna 1(shown in Fig1)

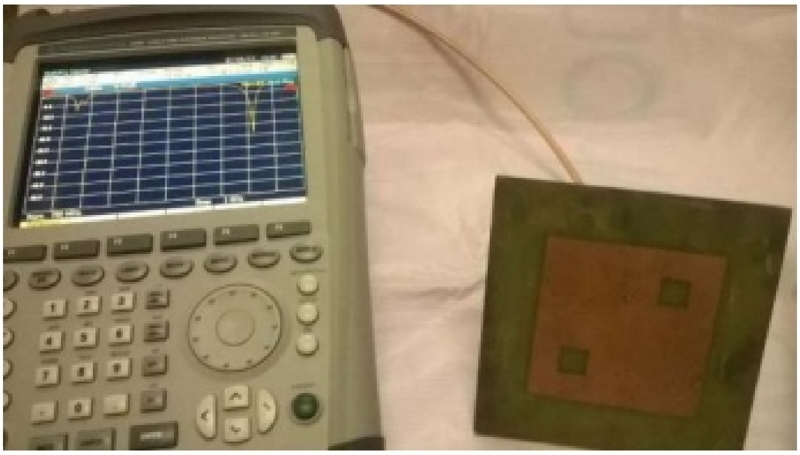

Fig 7. Fabricated Antenna of Fig 1 Antenna

It has been observed that the results so obtained for simulated and fabricated Antenna 1 are nearly matching with maximum 2% tolerance. This paper specifically discuss about the parameters like Axial ratio, Gain, VSWR, Return Loss @ 1 GHz as shown in Table 3, which are requirements for Circular Polarization of the patch antenna. Future studies are in progress for S and C band for mobile and wireless communication applications.

Parameters	Simulated Results	Fabricated Results
Gain (dB)	4.19	4.08
Return loss (dB)	-17.3	-17.1
Axial Ratio (%)	11.4%	10.6%
VSWR	1.26	1.31

Table 3. Results of Antenna 1 both with Simulated and Fabricated antenna @ 1GHz

IV. CONCLUSION

Four slotted antennas with various geometries were simulated using IE3D simulator, in which Microstrip patch antenna 1 (diagonally slotted two squares) was fabricated and compared with simulated results. The results so obtained are almost matching and perfectly suitable for patch antenna in L band, in considerations with circular polarizations. Future studies are still in progress to implement for patch antenna in other microwave band for mobile and wireless communication applications.

REFERENCE

[1] Yuan, X. Wang, and J. Chen, "A novel broadboad dual-band circular polarization stacked microstrip antenna, " I 0th International Symposium on Antennas, Propagation & EM Theo1y (ISAPE), pp. 366 - 368, Oct. 2012, DOI: LO.I 109/ISAPE.2012.6408787.

[2] Y. Ushjima, E. Nishiyama, I. Toyoda, and M. Aikawa, "Circular polarization switchable single layer microstrip array antenna" IEEE Propagation Society International Symposium, pp 1-2, July 2012 DOI: 10.1109/APS.2012.6348662

[3] T. Wu, H. Su, L. Gan, H. Chen, J. Huang and H. Zhang, "A compact and broadband microstrip stacked patch antenna with circular polarization for 2.45-GHz mobile RFID reader," IEEE Antennas and Wireless Propagation Letters, Vol 12 pp : 623 – 626, May2013, DOI: 10.1109/LAWP.2013.2261651.

[4] M.A. Rahman, Q. D. Hossain and M.A. Hossain, "Design of an x band microstrip array antenna for circular polarization, " IEEE International Conference on Electrical and Computer Eng, Dec2014, pp 184-187, DOl:10.1109/ICECE.2014.7026891.

[5] W. Ala and A. Z. Amro "Design and analysis of two E-shaped microstrip antennas with linear and circular polarization" IEEE 9th Int Symposium on Communication Systems, Networks & Digital Signal Processing (CSNDSP), 2014 , pp. 606 - 611, July 2014, DOI: 10.1109/CSNDSP.2014.6923900.

[6] Z. Muludi and E. Setijadi, "Design of circular polarization microstrip antenna circular dual-band on the frequency 145.9 MHz and 436.9 MHz for portable satellite earth station nano," IEEE 2015 Int. Electronics Symposium, pp.167-172, DOI: 10.1109/ELECSYM.2015.7380835.

[7] B. B. Dhengale and D. C. Karia, "A high gain 2-element microstrip array antenna with circular polarization for RFID application" IEEE 2015 Int. Conference on Advances in Computing, Communications and Infonnatics (ICACCI), pp. 116-120, DOI: 10.1109/ICACCI.2015.7275594.

[8] E. Nishiyama, A. Matsuo and I. Toyodo, "Double balanced multiplier integrated circular polarization switchable microstrip antenna" 2015 IEEE International Symposium on Antennas and Propagation & USNC/URSI National Radio Science Meeting IEEE, pp. 2239-2240, .DOI: 10.1109/RFIT.2016.7578150

[9] M. Yu, Longfang, Y. Chen, L. Zhang, H. Liu and Q. H. Liu, "Circular patch microstrip antenna with reconfigurable polarization capability" 2015 IEEE International Conference on Communication Problem- Solving (ICCP) IEEE, pp. 314-315, DOI: 10.1109/ICCPS.2015.7454160

[10] J C. J. Wang and W. B. Tsai, "Microstrip open slot antenna with broadband circular polarzation and impedance bandwith" IEEE Trans. on Ant. and Prop., 64(9), pp. 4095 – 4098, 2016, DOI: 10.1109/TAP.2016.2583459.

[11] Z. Pengfei, L. Shizhomg, C. Rongrong and H. Xinglin, "A reconfigurable microstrip patch antenna with frequency and circular polarization diversity" Chinese Jr of Elec., 25(2), pp. 379-383, March 2016. DOI: 10.1049/cje.2016.03.027

ISSN Print : 2320-2084, Online : 2321-2950

ULTRAWIDEBAND NOTCH ANTENNAS FOR WIRELESS APPLICATIONS

SANJEEV KUMAR YADAV, ABHISHEK SRIVASTAVA, SANJAY CHAUHAN
Department of Electronics and Communication Engineering, Institute of Engineering and Technology,Dr. Rammanohar Lohia Avadh University Ayodhya, U.P.-224001 India

A B S T R A C T

The ultrawide antennas are great demand for rapidly growth wireless communication system. The ultrawideband antenna covered wide bandwidth with lower power consume with coverage of short distance wireless communications. The planar microstrip antenna designed for UWB application due to its monopole feature, The monopole antenna consistsbandwidth and are preferred due to easy of fabrication low cost and light weight. The main disadvantage of UWB antenna is its interference with the undesired frequency bands. The undesired frequency bands are stopped by creating the notched of the undesired bands in the UWB bandwidth. The paper covered a review on UWB antennas with notches i.e., single bandnotch, dual band and triband notches. The notch in UWB antenna means that it rejects that frequency band. This paper is also explaining the design techniques for designing the notches in the UWB antennas. This paper will be helpful for the new researchers that want to work in the field of UWB notch antennas.

Keywords- UWB, Ultrawideband, Notch, Wireless Applications

I. INTRODUCTION

The antenna is passive device that convert electrical signal in to electromagnetic and vice versa. In the modern wireless communication system high speed data transmission and reception is needed that can be achieved by using wideband antenna, which can capable to operates multi-frequency of operations for different wireless applications.

The wide band antenna is not only capable to transmit data in high rate but also capable to operate multi frequency bands. This capability is achieved by designing low cost and less complex wideband/ ultrawideband antennas. The Federal Communications Commission allocated unlicenced ultra-wide band from 3.1 to 10.6 GHz frequency. The unlicenced ultra-wideband frequency band great demand in the researchers and scientist for designing the UWB antenna [1].

There are different types of UWB antennas and classified in term of planar and non-planar. The planar antenna is more popular now a day because easy to design, low cost and easy to integrated planar surface. The UWB antenna consists frequency interference with near frequency band.

In the UWB antenna there are several narrow frequency bands are utilized for several applications such as 3.3 to 3.6 GHz for WiMAX, 5.15 to 5.35 GHz, 5.725 to 5.825 GHz for WLAN applications[2]-[4]. For fulfilling the requirements of undesired frequency bands an antenna is desire that rejects the undesired frequency bands. Thus, an ultrawideband antenna withy multi notch capability is needed for different wireless applications.

II. VARIOUS TYPES OF UWB NOTCH ANTENNAS

2.1 Single Band Notch UWB Antenna

The single band ultrawide band notch antennas are most widely used such as in year of 2010, S. Barbarino et.al. [1] was designed a single notch UWB antenna by using an inverted-l notch for 5.0GHz WLAN band. This antenna is matched in 2.883 to 18.604 GHz and reject 4.844 to 6.190 GHz band. It has min. value of VSWR is 4.2 and maximum value is 19.3 over (5.150,5.825) GHz WLAN Band. It has smaller number of freedom and shows higher rejection of frequency band with 5G WLAN communication and in the year 2012, Shilpa Jangid, Mithlesh kumar.et.al. [5] has designed a UWB band notch antenna for WLAN and WiMAX applications. The antenna is designed using FR4 substrate with the dielectric constant of 4.4 and thickness of 1.6 mm and having size 15*14.5 mm2, fed with 50ohm return loss is less than 10 dB and show band notch to avoid interference caused by WLAN an WI-MAX. it has good omnidirectional coverage, stable transmission which indicates well suitability for integration into UWB portable devices, further, Nie fan, Jin long.et.al. [6] a microstrip antenna is integrated with a frequency reconfigurable second order stop bandfilter. The antenna works on the notch frequency band from 5.15 to 5.85 GHz provides filtering capability, for performing the filter operation a shape factor is placed. The antenna found good attenuation at notched band and achieved 0.72 shape factor for good filtration. The antenna is designed on multilayer structure, which provides sufficient gain with good shape factor. The antenna is designed on Fr4 substrate with small radiating patch and ground is connected with two resonator stubs. The designed antenna provides suitable band notch during the operating band. similarly, in the year 2019, Zhang et.al. [7] was designed a dual band dual polarized filtering antenna for WLAN Which covers the band notch from 3.4 to 3.6 GHz band. In the antenna filtering operation is achieved by modifying the dipole arm with the C shaped split rings and all of this happen without extra filtering circuit. The antenna covers 2.39-2.69 and 4.98-6.36 GHz frequency band with less than two VSWR and antenna achieved more than 7.5 dBi gain at lower frequency band and 9.7 dBi gain at higher frequency band in the next year Anees Abbas.et.al. [8] wasdesigned a compact rectangular notch UWB antenna for WLAN applications. The antenna is designed on TLY 5 A substrate and resonate at central frequency and controlled the notched bandwidth. The notch band characteristic was achieved by truncating the lower end of the patch with EBG structure. In the antenna notch and resonance frequency was tuned by changing EBG parameter. The antenna covered the size of 16*25*1. 52mm3.The antenna provides stable gain and radiation pattern. It having stable rectangular band notch band from 5-6 GHz for WLAN band and covered operational bandwidth from 3.1-12.5GHz. The band notch antenna and its returnloss are shown in figure 1.

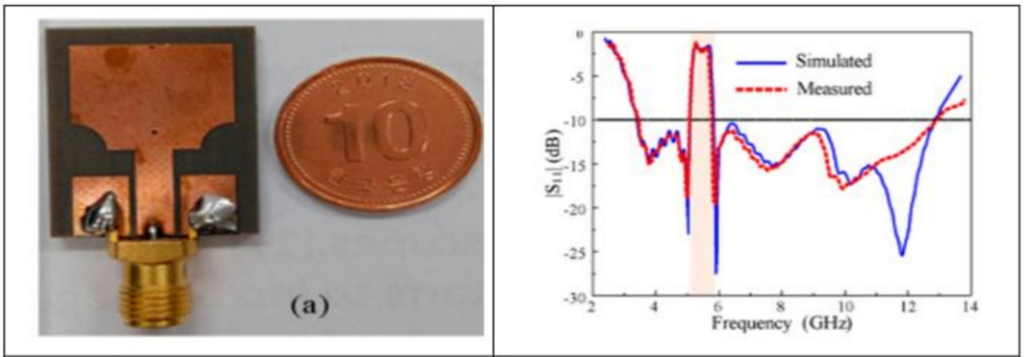

(a) (b)

Fig.1 (a) Top View of antenna (b) Return loss of the antenna [8]

In the year 2020, V N Koteshwara et. al. [9] is designed a compact triple band notched tapered microstrip fed UWB antenna for C, X & Ku band applications. The antenna is designed by elliptical patch with truncated ground plane. It covered the bandwidth of 3.1 to 18.8 GHz @-10 dB. During the UWB bandwidth, the antenna having three band notches at 3.7-4.2 GHz, 5.2-5.85 GHz and 8.0-8.4 GHz for C band, WLAN band, and X band applications. These notches are achieved by cutting three inverted U-shaped slots on the patch. The compact size antenna is suitable for mobile application and in the next year, Wahaj Abbas Awan et. al. [10] was designed a compact size printed UWBantenna using a genetic algorithm with notching characteristics for compact devices applications. The antenna covered frequency band from 3.75 to 4.85 GHz. The notch band of the antenna is achieved by etching two symmetrical slots from pentagonal radiating patch. The antenna covers the size of 20*15*0.508 mm3. The designed antenna resonant at 5.25 GHz and covered UWB with the fractional bandwidth of 180%. The UWB provides good return loss with omnidirectional radiation pattern. The summary of single band notch UWB antennas are given in table 1.

Ref No	Size (mm^2)	Design And Technique Used	Operating Frequency (GHz)	Band Notches (GHz)	Application
1	20.4x64	Inverted L-notch filter	5.1-5.8	(2.83,18.604) & (4.844,6.190)	5G WLAN Communication
5	15*14.5	Rectangular slot on radiating element	2.97-12.10	5.12-6.10	UWB portable devices
6	17*32	Shorted patch & ground jointed with two resonant stubs	3.1-10.6	5.15-5.85	------------
7	---------	Modifying dipole arm into C shaped split rings	2.39-2.69 4.98-6.36	3.4-3.6	WLAN applications
8	16*25	Truncating lower ends of patch & used EBG structure	3.1- 12.5	5-6	Biomedical imaging
9	16*26	Three inverted U-shaped slots on patch & truncated ground plane	3.1-18.8	3.7-4.2 for C band 5.2-5.85 for WLAN 8-8.4 for X band	Mobile applications
10	20*15	Two symmetrical slots from pentagonal radiating element	----------	3.75-4.85	W i MAX, WLAN, Sub-6GHz

Table 1. Summary of single band notch UWB antenna

Ultrawideband Notch Antennas for Wireless Applications

2.2 Dual Band Notch UWB Antenna:

There is extensively research has been done to design a dual band UWB antennas such as in the year 2016,Qi Lui et.al. [11] has designed a novel planar UWBfiltering antenna. it has dual notch characteristics in (5.5 & 7.5) GHz. The antenna is designed and simulate using HFSS software. The antenna designed on Taconic RF-35 substrate with the permittivity of 3.5, thickness 0.79mm, and loss tangent 0.02. The structure covered the size of 32*20 mm2. The dual notch UWB antenna was designed using half wavelength resonator structure with two U shaped gaps in coupler feeder. The antenna provides good impedance characteristics at the frequency of 3.5-10.5 GHz. The antenna reduces the interference between UWB antenna and other communication system forgood wireless applications and in the next year, Lin Chusan Tsai.et.al. [12] was designed a heptagonal shape monopole antenna for UWB application. It is designed on FR4 substrate with permittivity of 4.4, loss tangent of 0.0245, thickness 1.6mm. The proposed antenna covered the size of 26*16.38mm2. The antenna is designed on heptagonal shaped patch with cutting of two L shape slots and two SRRs on ground plane. The antenna covered the bandwidth from 2.63 to 10.86 GHz @VSWR< 2. The dual notch UWB antenna covers two notches for WiMAX and WLAN applications. The antenna provides good VSWR, radiation pattern and gain, Further Sam Weng Yik et. Al. [13] was designed a compact size reconfigurable dual notch band UWB antenna for RF /microwave front end subsystem. The UWB antenna is designed by two pairs of reconfigurable L shape resonator with T- shaped notch attached on partial ground plane. The antenna provides the smaller bandwidth 224.8 MHz and 89.90 MHz with the low input voltage of 6.0v used for RF /microwave front end subsystem. The dual band antenna and its return loss are shown in Figure 2.

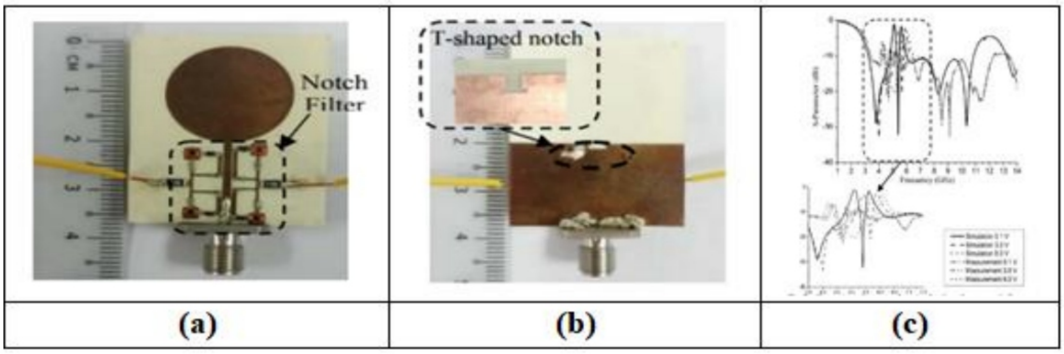

Fig.2. (a) Top view of the antenna (b) Bottom view of the antenna (c) Return loss of the antenna [13]

In the year 2019, A.K.M..Ariful et.al. [14] wasdesigned a compact planar UWB antenna forWiMAX and WLAN band notch applications. The antenna is designed by rectangular patch with slotted partial ground plane and for feeding the power micro strip feed line is used. The antenna covered the size of 30*12*1.6mm3. it used method of momentbased simulation technology. its operating band width from 2.98-12 GHz and gain is 3.95dBi. it has two notch bands at 3.5 &5.45GHz and have low cost &profile which used as transceiver in UWB communication and in the same year Abhishek Patel et. Al. [15] was designed ultra-wide band triband notches antenna for WLAN, WiMAX and X band rejection applications.

The antenna is designed on roger 5880 substrate with the dielectric constant of 2.2 and thickness of 0.795 mm. The antenna is designed by using monopole and covered 3.1 GHz to 10.6 GHz frequency band. In the antenna notches are inserted by using split ring esonators. The notches are resonated at 3.5 GHz, 5.8 GHz and 8.4 GHz for above band rejection applications. The antenna is designed and simulated by CST microwave software and in the next year a dual notch UWB coplanar waveguide antenna was designed by Ravichandran Somasundaram et. al. [16]. The antenna is designed on Rogers RT/duroid 5880substrate with dimension of 18*21*1.6mm3and feeding is done using 50ohm transmission line. The antenna covers dual notch bands 3.3-3.7 GHz and 5.9-6.9 GHz. The lower band notch is designed by an inverted pie section slot and higher band notch is designed using EBG structure for WiMAX and satellite uplink application. it can control frequency tunning easily .it used for reconfigurable antennas. Further in the last year 2021, Mubarak Sani Elliset.al. [17] was designed a notch bands antenna using vertical stubs from microstrip feedline. The designed UWB notch antenna solves the lack of details &replicable understanding the filtering techniques. it is etched on 25*30 mm2substrate. The two antenna structures are designed, in this design one narrow band notch lie from 3.3-3.6 GHz & second notch band from 5.15-6 GHz. The notch band provides good gain and group delay rejection. The antennaprovides stable radiation patterns with low cross polarization. The summary of dual band notch UWB antennas are given in table 2

S.No	Size (mm2)	Design And Techniques Used	Operating Frequency (GHz)	Band Notches (GHz)	Application
11	32*20	U shaped gaps in coupler feeder, half wavelength resonant structure	3.5-10.5	5.5 & 7.5	--------------
12	26*16.38	Two L-shaped slots on patch & two slot type split ring resonator on ground plane	2.63- 10.86	3.4-3.69 5.15- 5.85	UWB applications
13	37.6* 28	Two pair of reconfigurable L resonator & T-shaped notch attached on partial ground plane	3.048-10.561	5.2 & 5.8	RF/microwave front end subsystem
14	30*12	Rectangular patch & slotted partial ground	2.98-12	3.5 & 5.45	Transceiver in UWB communication
15	32×40	Monopole radiation patch with split ring resonators	3.1GHz to 10.6GHz	3.5 GHz, 5.8 GHz, and 8.4 GHz	short-range communication
16	18*21	Inverted π section slot & EBG STRUCTURE		3.3-3.7 5.9-6.9	Satellite uplink application Reconfigurable antenna
17	25*30	Vertical stubs protruded in feedline	3-10.6	3.3-3.6 5.15-6	-----------------

Table 2. Summary of dual band notch UWB antenna

2.3 Tri-Band Notch UWB Antenna:

There are extensively research going on for a tri-band notches UWB antenna, in the year of 2013, an ultra-wide band triband notch reconfigurable antenna was designed by Yingsong Li et. Al. [18] for Cognitive Radio Applications. The UWB notch antenna is designed with rectangular patch and band notches characteristic is obtained by inserting defective structure in the feedline with π shape slot cut from the radiating patch.

The ultrawide band antenna covers the frequency band from 3.1 GHz to 14.0 GHz band and covered the notch frequencies from 4.2 GHz to 6.2 GHz, 6.6 GHz to 7.0 GHz, and 12.2 GHz to 14 GHz. The antenna results show wide bandwidth, constant gain with omnidirectional radiation pattern and further in the year 2018, Qurratul Ain et.al. [19] had studied and analyzed the band notches characteristics for triple band notched UWB antenna.

A small square UWB antenna of size 24*31mm2 with triband rejection is designed and simulated using HFSS software. It reduced mutual coupling to the minimum among different slots placed on radiator without affecting the performance. The antenna provides an omni directional radiation in the H-plane for WPAN and other UWB applications. All these specifications justify that antenna is low cost, compact and ease to integrate in wireless devices.The proposed antenna and its return loss are shown in figure 3.

In the year of 2019, Abhishek Patel et.al. [20] has designed an UWB monopole with multiple band notches filtering antenna. It achieves better matching by creating a rectangular slot in ground plane and covers a range of 3.1GHz -10.6 GHz frequencies. Rejection levels at 5.8 and 8.4 GHz are below 3dB. Gain & efficiency are good for these frequencies. It is designed on CST microwave studio. Its application is in short range communication.

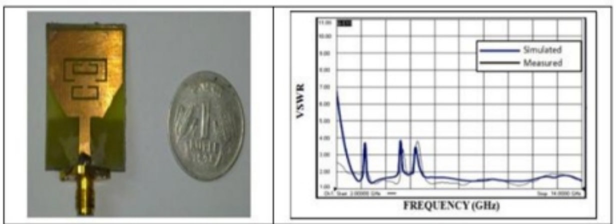

(a) (b)

Fig.3. (a) Antenna prototype (b) Return loss of the antenna [19]

Further Shun Li et.al. [21] was designed a triple notch fractal antenna with high selectivity characteristics for UWB applications. It is designed and simulated using HSFF software and covered the bandwidth upto 9.6 GHz. The antenna filters the three bands of 2.4G WLAN, 5G WLAN, and X-BAND uplink frequency without consuming more frequency bands. These notches are achieved by integrating different resonators at different parts of the antenna and in the year 2021, Warsha balani et. al. [22] was designed a compact triple band notch monopole antenna for wideband applications. The antenna is designed using E shaped stub, split elliptical shaped slot and C shaped resonator. The antenna covers the bandwidth from 1.6-47.5GHz with three notch bands at 1.8-2.2GHz,4-7.2GHz, and 9.8-10.4GHz for AWS, C, and X bands. it provides good radiation characteristics, constant group delay response, and better gain over passbands.

In the antenna during the notch bands low gain and high variation in group delay is achieved. So, it is suitable for pulse based SWB communication and in the same year a super wide band tri-band notches antenna was designed by Warsha Balani et. Al. [23] for wireless applications. The antenna was designed on roger RT duroid substrate with the dielectric constant of 2.2, and thickness of 1.57 mm. The radiating patch of the antenna consists labelled path with E shape stub connected to the patch and elliptical slot is etched from the lower end of the patch. The UWB antenna cover the bandwidth of 1.6 GHz to 47.5 GHz with the three notches of 1.8– 2.2 GHz, 4–7.2 GHz, and 9.8–10.4 GHz frequency for advanced wireless services (AWS), C bands, and X bands applications. The antenna consists good gain with radiation characteristic. The summary of Triband notch UWB antennas are given in table

III. CONCLUSION

This paper covered different categories of ultrawideband multi-notch antennas for different applications. For study the design techniques for creating the notch, different types of notch antennas are studies. These antennas are designed for reducing the interference with the narrow bandwidth channel. In these papers single band, dual band, tri-band notches in the UWB antenna are studied and identify the design techniques will be helpful for creation of notches in UWB antennas.

S.No	Size (mm2)	Design And Techniques Used	Operating Frequency (GHz)	Band Notches (GHz)	Applications
18	_	Defective microstrip structure in feedline & inverted π shaped slot in radiation patch	3.1-14	4.2-4.6 6.6-7 12.2-14	UWB cognitive radio communication
19	24*31	Different C and inverted C slots placed on radiator	3.1 - 14	3.3-3.7 5.1-5.4 5.7-6	UWB applications
20	32*40	Creating a rectangular slot in ground plane	3.1-10.6	5.8 & 8.4	Short range communication
21	55*50	C shaped slit, a CIDCLIR & CIDCLIR with extension line etched at intersection of feedline	1.2-10.8	2.4-2.6 5.05-5.8 7.83-8.44	-----------------
22	45*40	E-shaped stub, split elliptical shaped slot & C shaped resonator	1.6-47.5	1.8-2.2 4-7.2 9.8-10.4	Pulse based SWB communication
23	45×40	Labelled path with E shape stub connected to the patch and elliptical slot is etched from the lower end of the patch	1.6–47.5 GHz	1.8– 2.2 GHz, 4–7.2 GHz, and 9.8–10.4 GHz	Multipurpose Wireless Applications

Table 3. Summary of Tri-band notch UWB antenna

REFERENCE

[1] S.Barbarino, and F. Consoli: UWB circular slot antenna provided with an inverted-l notch filter for the 5 GHz WLAN band. Progress In Electromagnetics Research, PIER 104, 1–13 (2010).

[2] A.Gangwar and M. S. Alam: A high FoM monopole antenna with asymmetrical L-slots for WiMAX and WLAN applications. Microwave Optical Technology Letter, 60, 196-202 (2017).

[3] Ajay Kumar Gangwar and Muhmmad Shah Alam: A miniaturized quad-band antenna with slotted patch for WiMAX/WLAN/GSM applications. International Journal of Electrons and Communication (AeÜ), 112, 152911, (2019).

[4] A.K.Gangwar, M. S. Alam, V. Rajpoot, and A. K. Ojha: Filtering antennas: A technical review. International journal of RF and Microwave computer aided engineering, e22797, (2021).

[5] Shilpa Jangid, and Mithilesh Kumar: A Novel UWB Band Notched Rectangular Patch Antenna with Square slot. Fourth International Conference on Computational Intelligence and Communication Networks, pp. 5-9, IEEE, Mathura, India.

[6] K.V.Ajetrao, and A. P. Dhande: Phi Shape UWB Antenna with Band Notch Characteristics. Engineering, Technology & Applied Science Research, 8 (4), 3121-3125 (2018).

[7] Yaohui Zhang, Yonghong Zhang, Yong Fan and Daotong Li: Band-Notched Filtering Crossed Dipole Antenna Without Extra Circuit. IEEE International Symposium on Antennas and Propagation and USNC-URSI Radio Science Meeting, pp. 1135-1136, IEEE, Atlanta, GA, USA (2019).

[8] Anees Abbas, Niamat Hussain , Min-Joo Jeong , Jiwoong Park, Kook Sun Shin, Taejoon Kim and Nam Kim: A

[9] Rectangular Notch-Band UWB Antenna with Controllable Notched Bandwidth and Centre Frequency. Sensors, 20 (777), 1-11 (2020).

[10] Nam-I Jo, Dang-Oh Kim, and Che-Young Kim: A Compact Band Notched UWB Antenna for Mobile Applications. PIERS, 6 (2), 177-180 (2010).

[11] Wahaj Abbas Awan, Abir Zaidi, Musa Hussain, Niamat Hussain, and Ikram Syed: The Design of a Wideband Antenna with Notching Characteristics for Small Devices Using a Genetic Algorithm, Mathematics, 9 (2113), 1-13 (2021).

[12] Qi Liu, Chuansong Yu, Xianliang Wu, and Zhongxiang Zhang: A Novel Design of Dual-Band Microstrip Filter Antenna, IEEE Advanced Information Management, Communicates, Electronic and Automation Control Conference (IMCEC), pp. 1573-1576, IEEE, Xi'an, China (2017).

[13] Lin-Chuan Tsai: A ultrawideband antenna with dual-band band-notch filters. Microwave Optical Technology Letter, 59, 1861-1866 (2017).

[14] Sam Weng Yik, Zahriladha Zakaria, Noor Azwan Shairi: A Compact Design of Reconfigurable Dual BandNotched UWB antenna. IEEE International Workshop on Electromagnetics:Applications and Student Innovation Competitiion (iWEM), pp. 1-2, IEEE, Nagoya, Japan (2018).

[15] A.K. M. Ariful H. Siddique, Rezaul Azim and Mohammad T. Islam: Compact planar ultra-wideband antenna with dual notched band for WiMAX and WLAN. International Journal of Microwave and Wireless Technologies, 11(7), 1-8 (2019).

[16] Abhishek Patel and Manoj Singh Parihar: UWB Monopole Antenna with Triple-Band Notch Rejection. 2019 IEEE Conference on Information and Communication Technology (CICT), 1-4 (2019).

[17] Ravichandran Sanmugasundaram, Somasundaram Natarajan, and Rengasamy Rajkumar: Ultrawideband Notch Antenna with EBG Structures for WiMAX and Satellite Application. Progress In Electromagnetics Research Letters, 91, 25-32 (2020).

[18] Mubarak Sani Ellis, Philip Arthur, Abdul Rahman Ahmed, Jerry John Kponyo, Benedicta Andoh-Mensah, Bob John: Design and circuit analysis of a single and dual band-notched UWB antenna using vertical stubs embedded in feedline, Heliyon, 7 (12), e08554 (2021).

[19] Yingsong Li, Wenxing Li, and Qiubo Ye: A Reconfigurable Triple-Notch-Band Antenna Integrated with Defected Microstrip Structure Band-Stop Filter for Ultra-Wideband Cognitive Radio Applications. International Journal of Antennas and Propagation (2013).

[20] Qurratul Ain, Neela Chattoraj: Parametric study and Analysis of Band Stop Characteristics for a Compact UWB Antenna with Tri-band notches. Journal of Microwaves, Optoelectronics and Electromagnetic Applications, 7 (4), 509-527 (2018).

[21] Abhishek Patel and Manoj Singh Parihar: UWB Monopole Antenna with Triple-Band Notch Rejection. IEEE Conference on Information and Communication Technology, pp. 1-4, IEEE, Allahabad, India (2019).

[22] Shun Li, Shuxiang Song, Mingcan Cen, and Lihua Yu: Design of a high selectivity fractal antenna with triple bandnotched characteristics. International Conference on Microwave and Millimeter Wave Technology (ICMMT), pp. 1-3, IEEE, Shanghai, China (2020).

[23] Warsha Balani, Mrinal Sarvagya, Tanweer Ali, Ajit Samasgikar, Saumya Das, Pradeep Kumar, and Jaume Anguera: Design of SWB Antenna with Triple Band Notch Characteristics for Multipurpose Wireless Applications. Applied sciences, 11 (711), 1-21 (2021).

[24] Warsha Balani, Mrinal Sarvagya, Tanweer Ali, Ajit Samasgikar, Saumya Das, Pradeep Kumar and Jaume Anguera: Design of SWB Antenna with Triple Band NotchCharacteristics for Multipurpose Wireless Applications, Wireless Applications. Applied Science, 711, 1-21, 2021.

ISSN Print : 2320-2084, Online : 2321-2950

CONTROL OF AN AC CHOPPER BY A DIGITAL SIGNAL PROCESSOR USING A PROCESSOR-IN-LOOP ARRANGEMENT

DANIEL RIVERA, DAVID PLOMOZO, PAVEL ZUNIGA, DUNSTANO DEL PUERTO-FLORES
Graduate Program in Electrical Engineering, Dept. of Mech. and Electr. Eng.,CUCEI, University of Guadalajara, Guadalajara, México

A B S T R A C T

This document is aimed to present a processor-in-loop arrangement using the synchronous reference frame controller operating on an ac chopper for reactive and harmonic compensation. The controller is detailed taking into account the mathematical expressions of the converter, and how these shape its structure. The different harmonic components generated by the converter and how these are produced by specific duty-cycle components is also exposed. Finally, the implementation in a digital signal processor using a processor-in-loop arrangement to obtain transient- and steady-state signals aid in assessing the performance of the controller in cancelling both the reactive and selected harmonic components.

Keywords- AC Chopper, Synchronous Reference Frame, Processor-in-Loop Arrangement.

I. INTRODUCTION

Power quality is a key topic in power systems to maintain the energy supply under certain conditions to comply with power quality standards and help protect industrial processes and equipment. The most common power quality problems are low power factor and high harmonic distortion due to reactive and/or nonlinear loads mostly based on power electronics converters [1]. The impact of low power factor translates directly to reactive current having to be delivered to loads through distribution lines, which in turn increases power loss. On the other hand, harmonic distortion can causing negative effects in loads, like overheating of transformers, motors or conductors, among others [2].

The first solutions for power factor correction were synchronous condensers and capacitor banks, however, since loads usually vary, a fixed capacitor bank could lead to an insufficient or excessive compensation [3]. To aid in the performance of fixed filter banks, there are schemes for variable compensation using switched capacitors with the disadvantage of slow response, big size, and the need for frequent maintenance [1], there is also a method to deal with the reactive power incorporated in a nonlinear control framework [4].

A step forward was to increase the response time to half a cycle of the fundamental frequency by using phase controlled static var compensators (SVC), thyristor switched capacitors (TSC), or thyristor controlled reactors (TCR) to inject continuous reactive power [1]. One disadvantage is that when passing from injection to absorption of reactive power, or vice versa, the resonance angle and the surrounding regions must be avoided, also, the harmonic components generated have to be reduced [1].

The last step are self-commuted converters using pulse width modulation techniques (PWM) that can compensate power factor and harmonics at the same time [5]. Among these are voltage (VSC) and current sourced converters (CSC) or matrix converters (MC), among others. These can be used as building blocks for the static synchronous compensator (STATCOM) and its distribution version (DSTATCOM), the active power filter (APF)[5-6]. Additionally, to faster response times compared to thyristor-based converters, these can inject or absorb reactive power continuously, require smaller inductor or capacitor banks, and can also compensate harmonics [7]. These devices constitute a proven technology with limited penetration mainly because they require one or several inverters that still have bulky capacitor (or inductor) banks that considerably increase their cost[8].

From the vast universe of power converters, in 2007 Deepak D. [8] and Jyoti S. [9] publish a new concept using ac-ac converters for var and harmonic compensation. An advantage of not needing a VSC is to avoid bulky electrolytic capacitors in favor of ac capacitors, which reduces cost. Another advantage is the reduced number of power switches, typically three bidirectional switches in three-phase applications or the fact that the response speed is comparable to that of VSC [11]. These advantages have maintained interest in the research topic, for example, as a reactive and harmonic compensator with a Buck type ac chopper [10]; or with a Boost type ac chopper [11]. For harmonic compensation, the PWM scheme uses the even harmonic modulation technique (EHM) for the converter to be able generate the harmonic components that cancel the ones produced by a load[2], [8], [10]-[11].To find a solution capable of effectively and economically compensate power factor and harmonic distortion is desirable in practice, hence the use of ac choppers.

Additionally, the validation of the converter controller using a processor-in-loop (PIL) approach to accelerate the design process and avoid possible damages to a prototype or risk to operators is valuable. This type of simulation is intended to be the last step towards a laboratory prototype or an industrial test.This work is aimed to show the use of a processor-in-loop arrangement of a Buck type ac chopper for power factor and harmonic compensation of nonlinear and/or reactive loads under sinusoidal supply.

The specific objectives are:

1. Detailed operating principle of a Buck type ac chopper;
2. detailed operating principle of the control loop for power factor and harmonic compensation;
3. simulation of the entire system to assess its performance using a PIL arrangement.

II. OPERATION OF AN AC CHOPPER

The Buck type ac chopper can be modeled using a similar procedure as the matching dc-dc converter [10]. The conditions for the analysis consider power factor and harmonic compensation of a reactive/nonlinear load supplied by a sinusoidal voltage source. The configuration is shown in Fig. 1and consists of a voltage source, vs with an output impedance, Rs + jwl a second order input filter with elements Rf , Lf and Cf a power capicitor C with an inductive filter Lb; and two bidirectional power switches S1 and S2 [10]. The on/off sequence of the bidirectional power switches is complementary in a period of the commutation frequency, fsw as these cannot conduct at the same time.

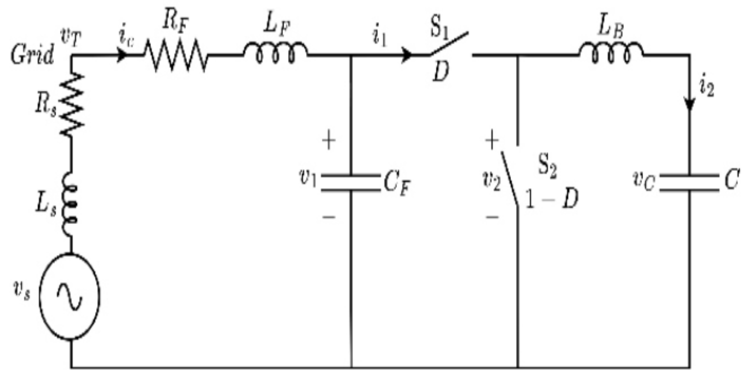

Fig. 1 Configuration of the Buck type ac chopper

2.1. Power Factor Correction

During converter operation it is supposed that the commutation frequency is sufficiently high for the voltages and currents to be represented by their average values, therefore v1 also the reactances of the elements are selected to be much smaller than that of making behave as ideal filters. From [[1]] and according to the volts-seconds and power balance, v2 and i1 can be expressed as

$$v_2(t) = d(t)\, v_1(t),\ i_1(t) = d(t)\, i_2(t); \qquad (1)$$

considering (1) and that $v_C(t) \cong v_2(t)$and $i_c(t) \cong i_1(t)$, it follows that i_2 and i_c are given by

$$\begin{aligned} i_2(t) &= d(t)C\frac{\mathrm{d}v_T(t)}{\mathrm{d}t} + v_T(t)C\frac{\mathrm{d}d(t)}{\mathrm{d}t} \\ i_c(t) &= d^2(t)C\frac{\mathrm{d}v_T(t)}{\mathrm{d}t} + v_T(t)d(t)C\frac{\mathrm{d}d(t)}{\mathrm{d}t} \end{aligned} \qquad (2)$$

The compensation current ic depends on both the duty cycle d(t) and the voltage at the point of common coupling (PCC) vr(t) therefore considering a fairly constant sinusiodal node voltage and a steady state duty cycle can be rewritten as

$$\begin{aligned} v_2\ (t) &= \ D_0 V_m \sin(\omega t + \varphi) \\ i_c(t) &= (D_0)^2 C\omega V_m \sin\left(\omega t + \varphi\ + \frac{\pi}{2}\right). \end{aligned} \qquad (3)$$

It is clear that ic leads vr by 90 degree and that D controls its amplitude providing a variable capacitive current to compensate for the inductive current of a given load fig 2a shows that effect of D in the amplitude of ic

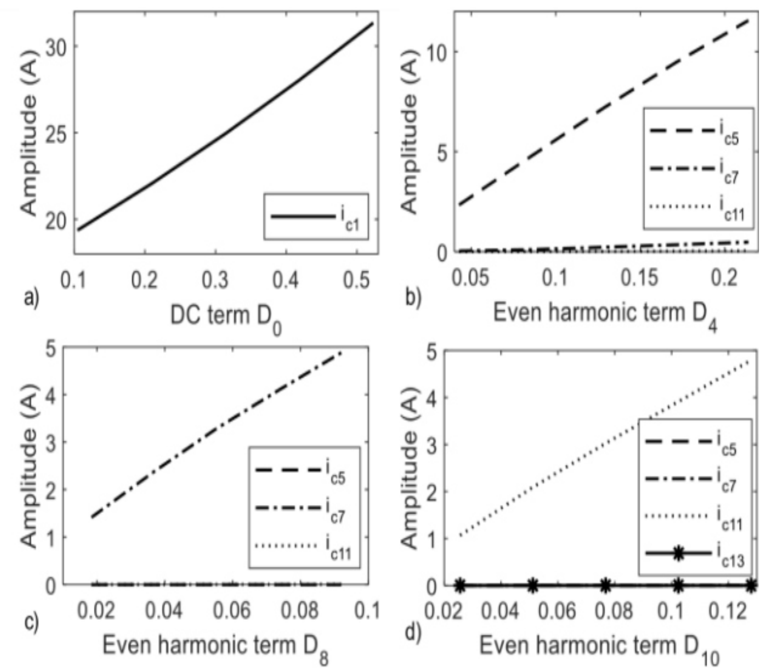

Fig. 2Amplitude of different frequency components of i_c against a) D_0, b) D_4, c) D_8, and d)D_10

2.2. Harmonic Cancellation

Harmonic behaviour is studied by a procedure as the one above allowing d to have an ac component as in d(t) = D0 + Dk sin(kwt + 0k) can therefore be modified and give

$$v_2(t) = D_0 V_m \sin(\omega t + \varphi) + \frac{D_k V_m}{2}\left[\cos\left((k-1)\,\omega t + \theta_k - \phi_1 + \frac{\pi}{2}\right) - \cos\left((k+1)\omega t + \theta_k + \phi_1 - \frac{\pi}{2}\right)\right]; \quad (4)$$

$$i_c(t) = \omega C V_m \left\{\left(D_0^2 + \frac{D_k^2}{2}\right)\sin\left((k-1)\omega t + \theta_k - \phi_1 + \frac{\pi}{2}\right) + D_0 D_k\left[\frac{k-2}{2}\sin\left((k-1)\omega t - \theta_k - \phi_1 + \pi\right) + \frac{k+2}{2}\sin\left((k+1)\omega t + \theta_k + \phi_1\right)\right] + D_k^2\left[\frac{k-1}{4}\sin\left((2k-1)\omega t + 2\theta_k - \phi_1 + \frac{\pi}{2}\right) + \frac{k+1}{2}\sin\left((2k+1)\omega t + 2\theta_k + \phi_1 - \frac{\pi}{2}\right)\right]\right\}.$$

It is clear that ic includes the harmonic terms $(k-1)^{\text{th}}$, $(k+1)^{\text{th}}$, $(2k-1)^{\text{th}}$ and $(2k+1)^{\text{th}}$ with different magnitude the highest being the (k + 1)th term followed by the (k-1)th therefore if a kth even harmonic term is included in d it will generate the (k + 1)th harmonic current in ic to cancel an odd harmonic component at the PCC. This is known as EHM and consist on injecting even harmonic terms in d to produce odd harmonic currents in an ac chopper.

Typical harmonic currents in balanced three-phase systems include the 5th, 7th , 11th, 13th, 17th, 19th, ..., note that the three-phase balanced system lacks the 3rd harmonic component and its multiples. These components can be cancelled including appropriate even harmonic terms as in d(t) = D0 + $\sum_k D_k \sin(k\omega t + \theta_k)$, where k is an event term that generates the (k+1)th harmonic current in Ic. To show this, let us include a single even harmonic term in d and observe the odd harmonic current generated in ic ; as an example, Fig. 2b, c, and d show the components of ic produced by the 4th , 8th terms in d; it is clear that one harmonic component has the dominant magnitude for each even term injected.

III. SYNCHRONOUS REFERENCE FRAME CONTROLLER

The test system is shown in Fig. 3and comprises a voltage source $v_s = V_{s_{L-L}} \sin(\omega_s t + \phi_s)$ with a linking impedance $R_s + j\omega L_s$; two linear loads with impedances $R_1 + j\omega L_1$ and $R_2 + j\omega L_2$; an uncontrolled rectifier with a dc load given by Rdc1 , Rdc2 and Ldc; and a three-phase ac chopper with a per phase configuration as the one in Fig. 1; the parameters of the test system are $V_{s_{L-L}} = 220$ V rms, $\omega_s = 2\pi 60$ rad/s, $\phi_s = 0°$, $R_s = 0.001\ \Omega$, $L_s = 10\ \mu$H, $R_1 = 4\ \Omega$, $L_1 = 18\ \mu$H, $R_2 = 3\ \Omega$, $L_2 = 10.5\ m$H,$L_2 = 10.5\ \mu$H, $R_{\text{dc}_1} = 12\ \Omega$,$R_{\text{dc}_2} = 6\ \Omega$, $L_{\text{dc}} = 200\ \mu$H,$R_{\text{F}} = 1\ \Omega$, $L_{\text{F}} = 160\ \mu$H, $C_{\text{F}} = 80\ \mu$F, $L_{\text{B}} = 180\ \mu$H, $C = 660\ \mu$F, and $f_{\text{sw}} = 12$ kHz. It is common in electrical engineering applications to use the synchronous reference frame (SRF) for different tasks since it transforms an ac vector in abc coordinates into a constant vector in dq0 coordinates. In control systems, for example, it makes the use of proportional-integral (PI) controllers easier. The control system used in this work is based on this abc-dq0-abc transformation and in shown inFig. 3, where the reactive and harmonic sections are identified.

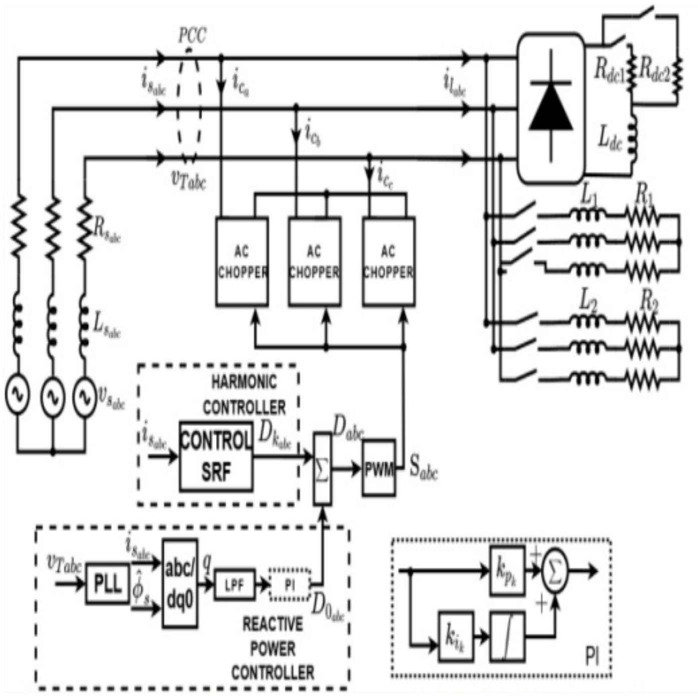

Fig. 3Test system with nonlinear-reactive load and ac chopper.

3.1. Reactive Power Controller

Following the ideas in the previous section, the reactive power controller is based on the abc-dq0 transformation to obtain the information of the reactive power of the load. When the load is linear the abc current abc current drawn is sinusoidal and when converted to the dq0 frame the dq components are constant and contain key information of the current. Moreover, if the phase of the transformation matrix, is synchronized with vr these d and can be related to active and reactive power, respectively. This is used here to compensate the reactive power of the load by driving the q component of is to zero zero using a PI controller as the one shown inFig. 3, thus reducing the reactive power at the PCC. The d component is not affected since it is related to the active power. The synchronization waveform $\delta = \omega_\delta t + \phi_\delta$, for the abc-dq0 transformation contains the data of the frequency and phase of the synchronizing signal and is obtained using a SRF phase-locked loop (PLL), like the shown in Fig. 4,as it is one of the most used schemes [1]. As mentioned before, the linear load results in a purely sinusoidal current, and for the transformation matrix to be synchronized with the voltage at the PCC

$$\omega_\delta = \omega_s \text{and } \phi_\delta = \hat{\phi}_s.$$

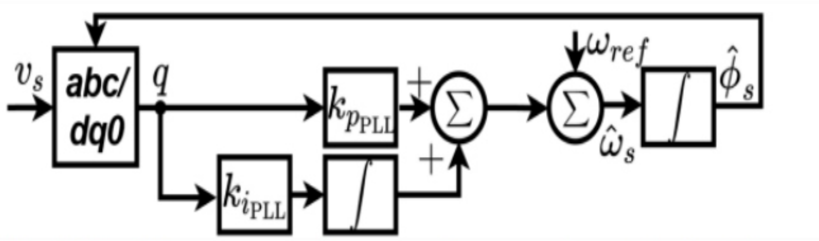

Fig. 4Synchronous reference frame phase-locked loop.

As shown inFig. 3, the controller transforms is from the abc to the dq0 reference frame. The q component is then passed through a low-pass filter to reduce the high frequency switching harmonics of the ac chopper and become the error signal of the controller that outputs the duty-cycle. The data for the reactive controller is kpdc = 0.5 and kidc = 5 and from the PLL is kppl = 100 and kipll = 1.

3.2. Harmonic Controller

With a nonlinear, the abc current drawn from the source becomes distroted and can be represented as $i_s = \sum_{k=1}^{\infty} A_k \sin(k\omega t + \phi_k)$, where Ak is the amplitude of the kth harmonic component and is its phase ; remember that for the test system used k = 5,7,11,13.... When is is converted to the dq frame it results in isdq + isdq where isdq is a constant (dc) component and isdq is an alternate (ac) one.

The synchronization waveform for each transformation, in Fig. 5is not obtained from a PLL, but specifically generated for each control loop. This determines the components of isdq where Isdq from is= Ak sin (kwt + k) when wsn = kw and isdq results from the rest of the components when wsn not equal to kw. In this case, the phase of the transformation, the does not need to be synchronized since any distortion of the voltage at the PCC is supposed to be negligible, therefore no harmonic components of the current can be paired with harmonic components of the voltage.

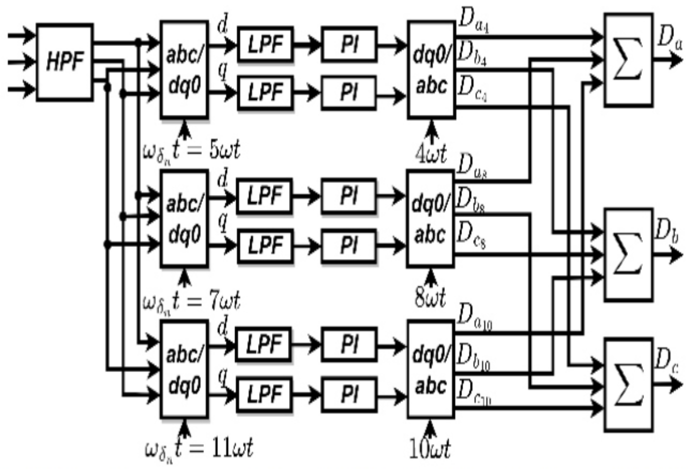

Fig. 5Synchronous reference frame harmonic controller.

Fig. 5shows the detail of the harmonic controller composed of a series of harmonic loops, where one targets a specific harmonic component generated by the load. All harmonic loops have a common structure that begins with is being passed through a high-pass filter to reduce its fundamental frequency component, as this is the one with the highest magnitude. The current is then transformed to the dq reference frame to be fed to a low-pass filter to diminish any ac components. This signal contains the information of a specific harmonic component and is used as the error input for the controller. Finally, the output of the controller is converted back to the abc reference frame to be added to the constant duty cycle. Note that the abc-dq0 and dq0-abc transformations in each harmonic loop are synchronized to different frequencies. The frequency of each transformation block is determined by harmonic component that the corresponding controller needs to process, and the component that needs to be injected by the ac chopper. As shown in Section II, the injection of different even harmonic terms to the duty-cycle results in the ac chopper injecting a specific odd harmonic current.

To further clarify, and without loss of generality, let us concentrate on id as the same applies to iq. Also, let us focus on the control loop of the 5th harmonic component, as a similar process applies to the other loops. The control loop starts with a high-pass filter to reduce the fundamental frequency component of is The filtered current is then converted to the dq reference frame with wsn matching the 5th harmonic component. Hence, Id is only linked to the 5th harmonic component, whereas id results from the fundamental frequency and the rest of the harmonic components; note that this means that to compensate for the 5th harmonic component only id is needed. Therefore, the next step is to reduce id using a low pass filter for the PI controller to process a dc signal. Finally, when converting the output of the controller to the abc reference frame wsn is set to the 4th component since it has already been shown that when included in d(t) it generates a 5th harmonic current component in the ac chopper (Fig. 2b).

Accordingly, the frequency of the dq transformation for the controller loop of the 7th and 11th harmonics are set to these frequencies for Idq to contain the appropriate information; in both cases idqs filtered before entering the PI controller. Finally, when transforming back to abc cordinates the frequency of the transformations match the 8th and 10th terms that will generate the7th and 11th harmonic currents in ic. As a final but very important remark, one can note that the 8th term is used to generate the 7th component in ic , i.e the (k + 1) term to generate the kth harmonic. However, this is not the case for the other two control loops, where the 4th and 10th terms are used to generate the 5th and 11th components in ic respectively, i.e the (k-1)th term to generate the kth harmonic. The reason lies in the 7th harmonic component to be of positive sequence, whereas the 5th and 11th are of negative sequence. The duty-cycle that generates a positive or negative sequence harmonic component in ic is not the same, and has

to be properly selected, as shown in Fig. 5.The harmonic controller parameters are kp4= 0.02 , ki4 = 0.45 , kp8 = 0.014 , ki8 = 0.5 , kp10 = 0.062 , and ki10 = 3.1.
The high- and low-pass second order filters are given by

$$\frac{i_{s_f}(z)}{i_s(z)} = \frac{b_0 z^2 + b_1 z + b_2}{z^2 + a_1 z + a_2}$$
$$\frac{i_{dq_f}(s)}{i_{dq}(s)} = \frac{\omega_c^2}{s^2 + 2d_r\omega_c s + \omega_c^2} \quad (5)$$

respectively, with the filter configurations presented in Fig. 6. The high-pass filter is directly represented in a block diagram with delays, and the low-pass filter is achieved using its transfer function with discrete integrators. The data of the filters is b0 = 0.9868, b1 = 1.9735 , b2 = 0.9868 , a1 = - 1.9733 , a2 = 0.9737 , $\omega_{c_{dc}} = 2\pi 45$, $d_{r_{dc}} = 2$, $\omega_{c_4} = 2\pi 60$, $d_{r_4} = 0.7$, $\omega_{c_8} = 2\pi 60$, $d_{r_8} = 0.7$, $\omega_{c_{10}} = 2\pi 25$, $d_{r_{10}} = 2$.

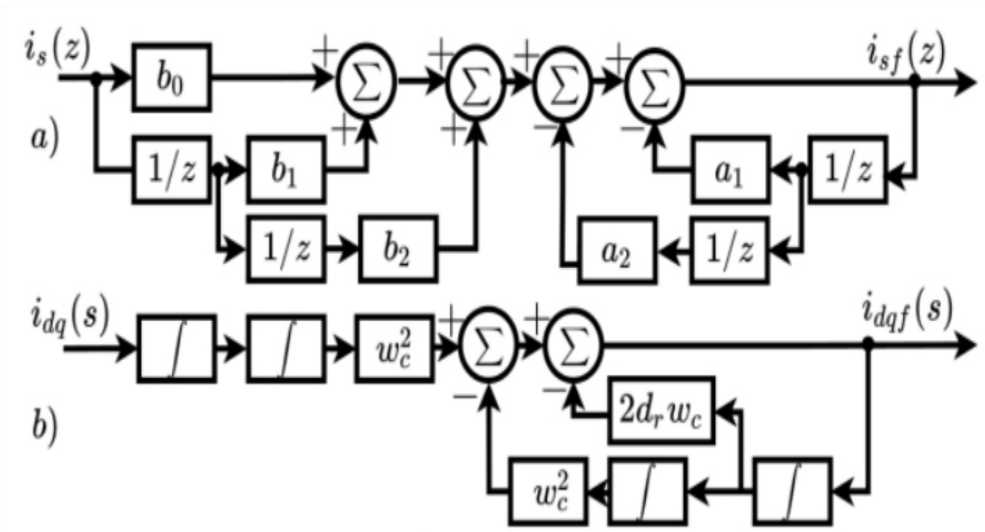

Fig. 6Schematic diagrams for the a) high-pass filter, and b) low-pass filter.

IV. PROCESSOR-IN-LOOP SIMULATION RESULTS

This section shows the results when using the test system of Fig. 3 with an actual Texas Instruments TMS320F28335®processor board running the controller. The test is performed with the PIL function of the PSIM® software that allows to connect a processor hardware to a digital simulation. In this test, the board runs at a sampling frequency of 20 kHz(50 us sampling time).This PIL function allows to assess the performance of the controller since it runs each sample time in real-time on the processor board, however, the data exchange between processor and computer simulation is not in real time.The results shown include four cases for the controller: a) reactive controller, b) reactive controller and the 5th harmonic loop, c) reactive controller, 5th, and 7th harmonic loops, and d) reactive controller, 5th, 7th,and 11th harmonic loops.

All simulations start in steady-state with the ac chopper connected and the ac load being R1 + jwl;, then at t = 0.1 sthe ac load changes to R2 + jwl2 and the dc load Rdc1 - Ldc1 is connected ; finally at t = 0.35 s the ac load remains at R2 + jwl2 and the dc load changes to Rdc2 - Ldc. The objective of the tests is to show the effect of each control loop in Is and the specific components affected. For all tests the signals shown are vT , is , il , and ic; the harmonic spectrum of is , il , and ic are also presented.

Fig. 7shows the behavior with the reactive loop, where is clear that vT and is are in phase, meaning that ic is compensating the reactive power even when the load changes; the system is observed to rapidly reach the steady-state. It is also clear from Fig. 8 that ic is sinusoidal even when the nonlinear load is connected and is gets distorted. The harmonic content that appears is not cancelled by the reactive controller and will remain as long as the nonlinear load is connected.

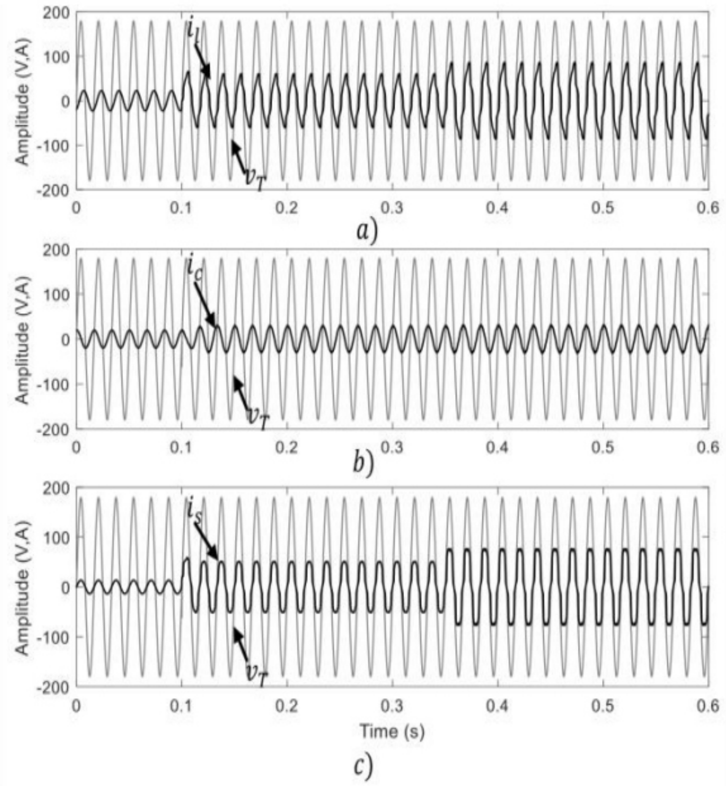

Fig. 7Variables with Q control loop.

A different behaviour is shown inFig. 9, where the reactive and 5th harmonic control loops are present. The reactive control loop plays the same role as in the previous test; however, it is now clear that is is less distorted due to the action of the harmonic loop; again, the system rapidly reaches the steady-state.The harmonic spectrum plotted in Fig. 10reveals the effectiveness of the additional loop, where the 5th harmonic component of is is now cancelled; other components will be cancelled adding more loops.

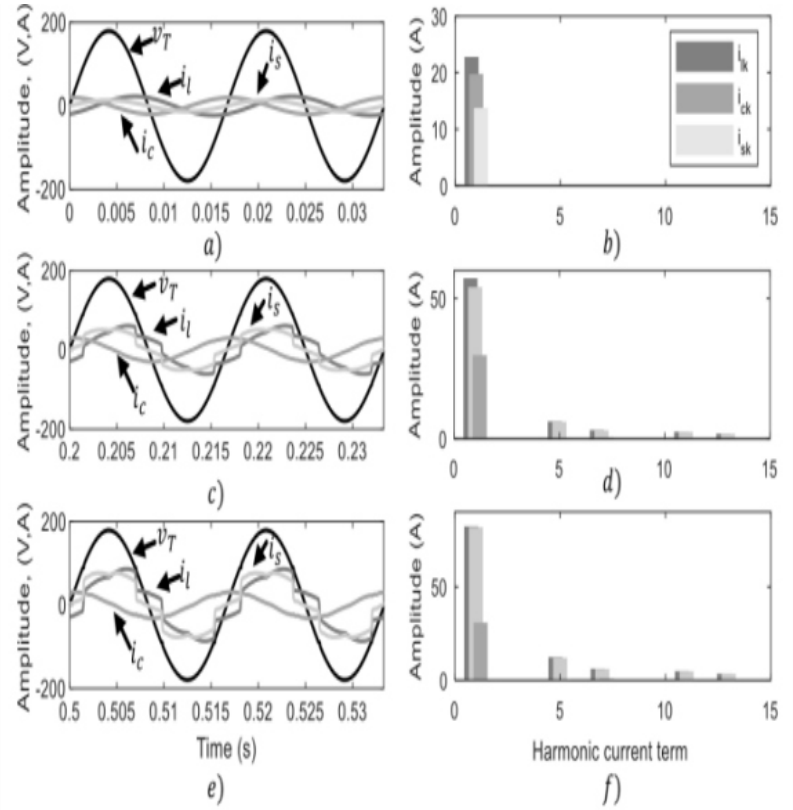

Fig. 8Harmonic spectrum with Q control loop.

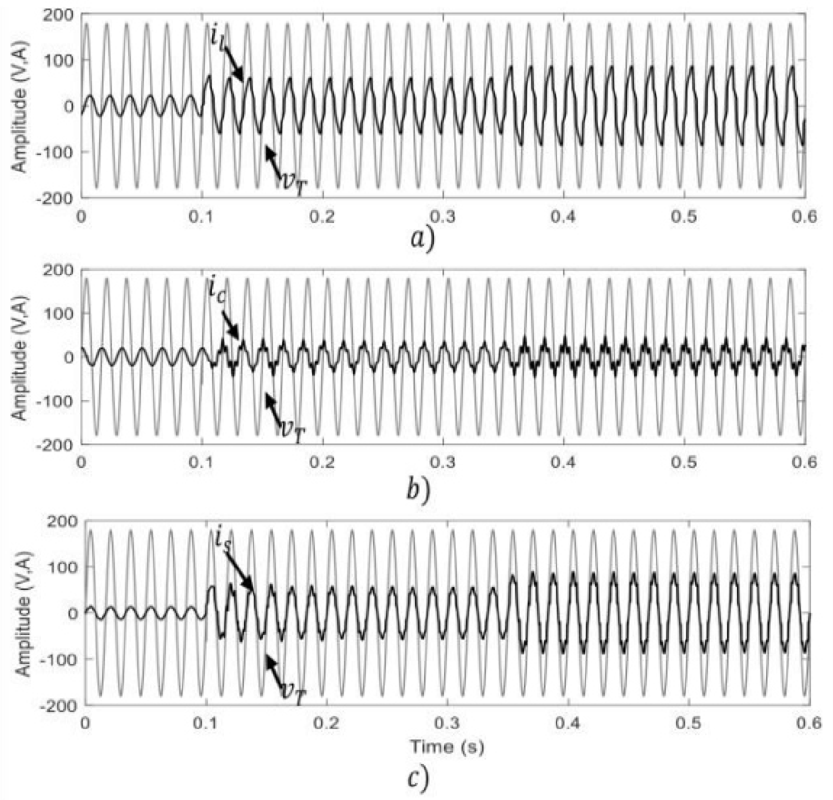

Fig. 9Variables with Q and 5^thharmonic loop.

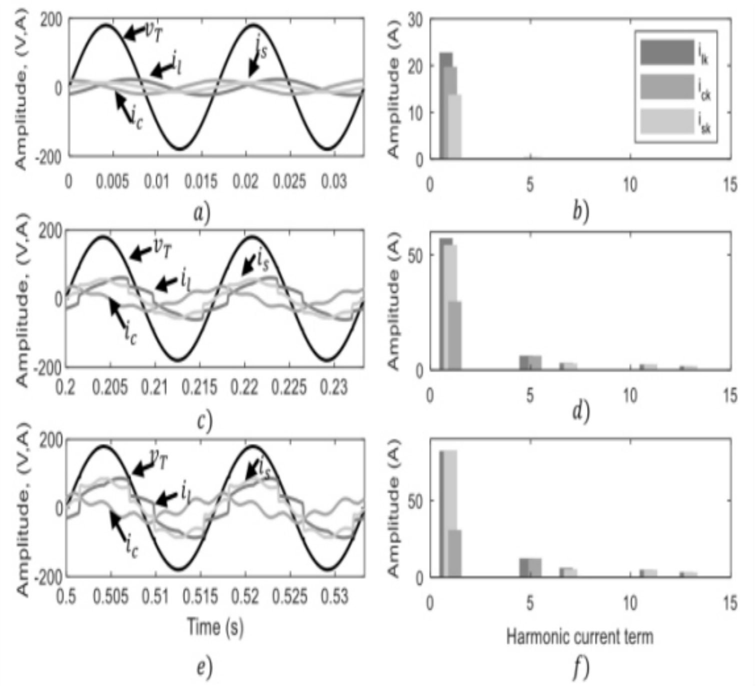

Fig. 10Harmonic spectrum with Q and 5^thharmonic loop.

In line with the previous tests, Fig. 11shows the effect of adding the 7th control loop. The results follow the same logic and the 7th harmonic component is effectively cancelled from is with the system rapidly reaching the steady-state. The utility of the additional loop is exposed inFig. 12, where the harmonic spectrum lacks the 7th harmonic component. Finally, adding the 11th harmonic control loop helps to neutralize the corresponding harmonic component, as depicted in Fig. 13.The distortion in is is further reduced as clearly shown in the harmonic spectrum of Fig. 14.Very little distortion is present in is is in phase with vT.

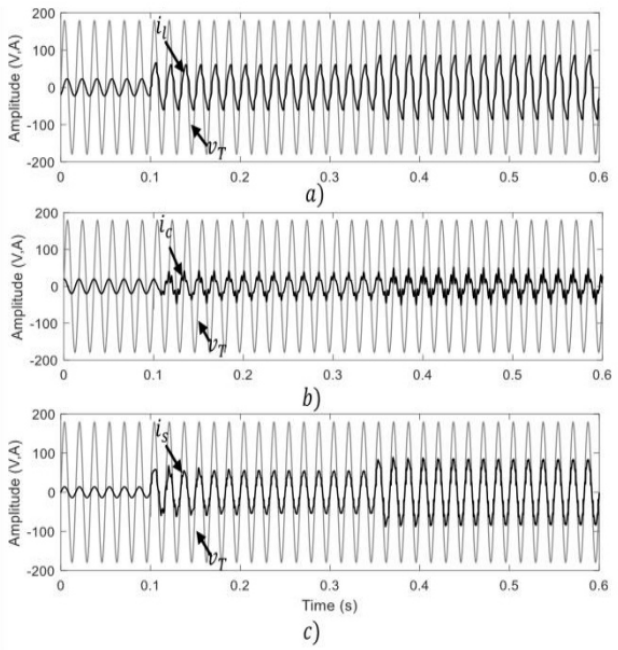

Fig. 11Variables with Q5^th, and 【7】^thharmonic loop.

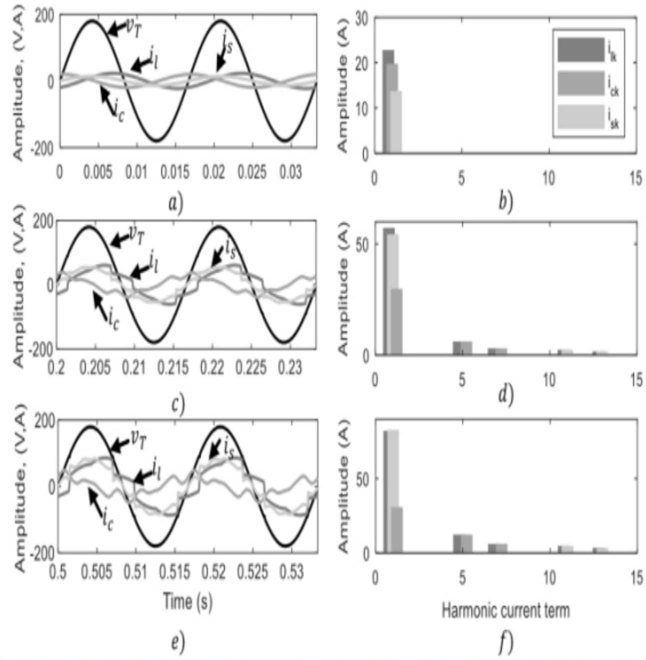

Fig. 12 Harmonic spectrum with Q, 5^thand7^thharmonic loop.

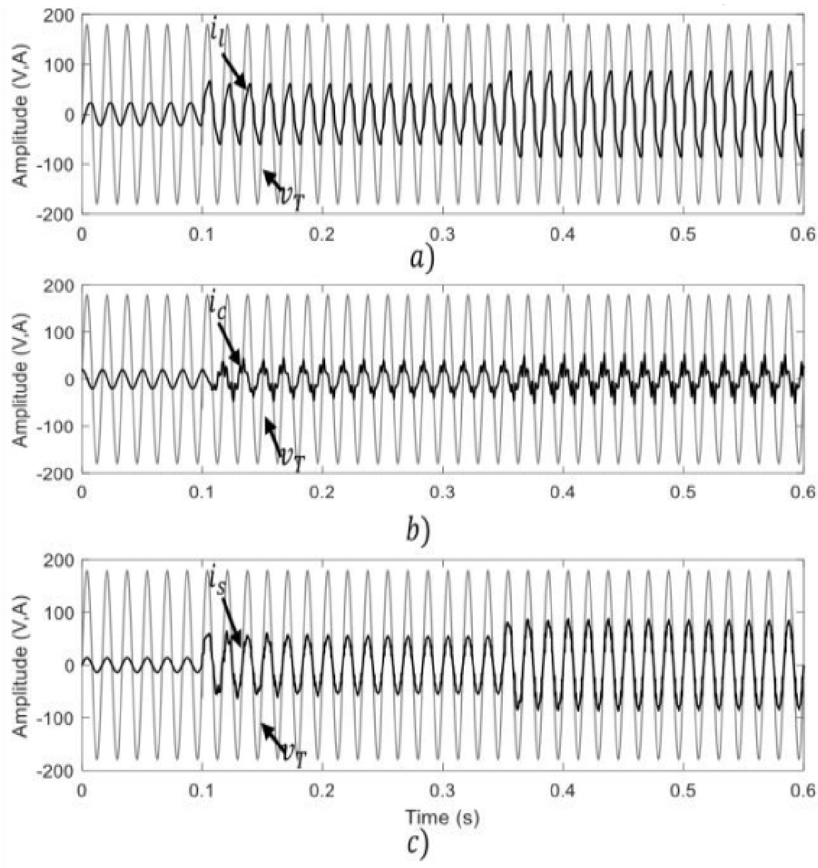

Fig. 13Variables with Q, 5^th, 7^thand【11】^thharmonic loop.

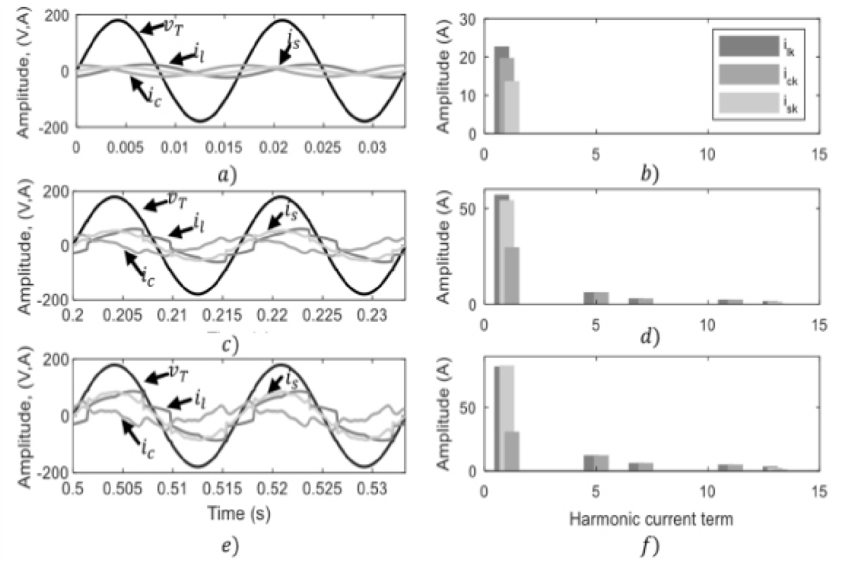

Fig. 14Harmonic spectrum with Q, 5^th, 7^thand【11】^thharmonic loop.

Since the tests presented account for an actual processor handling the control system, running times are an effective way of assessing the real-life performance of the system. For the reactive, reactive and 5th , reactive, 5th and 7th , and reactive, 5th,7th and 11th control loops, the processing times are 5.15 us , 16.6 - 18.3 us, 26.7 - 28.4 us and 36.5 - 38us , respectively. It is important to note that all these running times are safely below the 50 us sampling time used in all tests.

V. CONCLUSION

The SRF is an effective way to design a controller that needs to separate different harmonic components. However, in the case of the ac chopper with EHM one has to take special care on the frequency of the abc - dq0- abc transformations since the sequence of each harmonic component has to be considered, otherwise the controller will not behave as desired.

On the other hand, performing a PIL simulation has the advantage of testing the controller in a form that is close to the actual implementation since the processor is effectively running the algorithms; all that is needed to switch to a prototype is to acquire actual measurements.

REFERENCE

[1] J. Dixon, L. Moran, J. Rodriguez, and R. Domke, "Reactive power compensation technologies: state-of-the-art review",Proc. IEEE, vol. 93, no. 12, pp. 2144-2164, 2005.

[2] Prasai, J. Sastry, and D. Divan, "Dynamic var/harmonic compensation with inverter-less active filters," IEEE Ind. Appl. Society Annual Meeting, pp. 1-6, 2008.

[3] H. Frank, and B. Landstrom, "Thyristor-controlled shunt compensation in power networks," ASEA Journal, vol. 54, pp. 121-127, 1981.

[4] D. del Puerto-Flores, R. Ortega, and J. M. A. Scherpen, "On power factor improvement by lossless linear filters under nonlinear nonsinusoidal conditions," PrzegladElektrotechniczny, vol. 87, no. 1, pp. 112-117, 2011.

[5] B. Singh, K. Al-Haddad, and A. Chandra, "A review of active filters for power quality improvement," IEEE Trans. Ind. Electron., vol. 46, no. 5, pp. 960-971,1999.

[6] W. Rohouma, R. Balog, A. Peerzada, and M. Begovic, "DSTATCOM for harmonic mitigation in low voltage distribution network with high penetration of nonlinear loads," Renewable Energy, vol. 145, pp. 1449-1464, 2020.

[7] F. Peng, L. Chen, and F. Zhang, "Simple topologies of PWM AC-AC converters," IEEE Power Electron. Lett., vol. 1, no. 1, pp. 10-13, 2003.

[8] D. Divan, and J. Sastry, "Inverter-less active filters - a new concept in harmonic and var compensation," IEEE Power Electron. Specialists Conf., pp. 2926-2932, 2007.

[9] D. Divan, and J. Sastry, "Voltage synthesis using dual quadrature sources - a new concept in AC power conversion," IEEE Power Electron. Specialists Conf., pp. 2678-2684, 2007.

[10] X. Chen, K. Dai, Y. Zhang, L. Peng, and Z. Dai, "Interaction and coordination between reactive compensation and harmonic suppression for three-phase buck-type D-CAP," IET Power Electron., vol. 12, pp. 2953-2964, 2019.

[11] Q. Liu, Y. Deng, and X. He, "Boost-type inverter-less shunt active power filter for VAR and harmonic compensation," IET Power Electron., vol. 6, pp. 535-542, 2012.

ISSN Print : 2320-2084, Online : 2321-2950

PERFORMANCE ANALYSIS AND COMPARISON OF APD AND PIN PHOTODETECTORS USING OPTICAL WIRELESS COMMUNICATION CHANNEL

ARAFAT A. A. SHABANEH
Lecturer, Department of Telecommunication Technology Engineering, Faculty of Engineering and Technology, Palestine Technical University–Kadoorie (PTUK), Tulkarm, Palestine

A B S T R A C T

Owing to the high commercial demand for optical communication system, the fundamentals of avalanche photodiode (APD) and photodiode intrinsic negative (PIN) of receiver performance have received extensive attention. This work presents a performance analysis and comparison of APD and PIN photo detectors using optical wireless communication channel. Many parameters are investigated to study the effects of input power, extinction ratio, gain, thermal noise, bandwidth, and dark current. Results show that APD photodiode shows high Q-factor, which is mainly affected by gain and thermal noise, whereas PIN photodiode is influenced by thermal noise. Moreover, the APD's gain acts anessential role, and the shot noise has to be carefully dealt with. The implementation of APD photodiode in optical communication system exhibited high Q-factor of 257 for long transmission distance of up to 300 km compared to PIN photodiode with Qfactor of 219. Furthermore, the correlation of receiver sensitivity with extinction ratio and thermal noise is examined and compared.

Keywords- OWC channel, PIN, APD, Q-factor, thermal noise, shot noise, gain, extinction ratio

I. INTRODUCTION

Optical receivers are highly attractive and widely used in the field of communication engineeringbecause they are considered the major devices in optical communications system [1-5]. Avalanche photodiode (APD) and photodiode intrinsic negative (PIN) photo detectors are the fundamental component of the optical receiver, andthey operate close to 1.5 μm spectral range [3]. On the one hand, APD photodetectors are the better candidate for long-haul communications, because of their internal gain. On the other hand, the thermal noise in PIN photodiode acts the main function in the performance of the receiver [1-3].

Currently, the focus of conventional communication systems has shifted to fiber optic systems in aspects of proper usage of bandwidth and the enhancement of capacity [4-5].Optical wireless communication channel (OWC) is a technology that applies light to transmit optical signals over free space. OWCchannel is implemented to handle data at very high

$$i_{AYAL}^2 = i_{thermal}^2 + i_{av}^2 = 2e\left(I_{ph} + I_B + I_D\right)BM^2F + \frac{4kTB}{R} \qquad (1)$$

data rates, and it is available at a very low cost compared to other telecommunication systems [2-3].

Numerous studies have aimed to investigate the performance comparison between APD and PIN photodetectors at the receiver side.O. Kharraz and D. Forsyth [1] demonstrated a performance comparison of the conventional PIN photodiode with the APD in an optical communication system.

They studied and compared comprehensively the effects of bandwidth, gain, extinction ratio, shot noise, and thermal noise. Furthermore, they proved that the Q-factor value is affected by the thermal noise in the PIN, and by the thermal and shot noise in the APD photo detector.They also showed that the APD's internal gain performs a substantial role in the receiver evaluation.

The evaluation quality of an optical communication system is progressed via Q-factor, bit error rate (BER), electrical and optical power, RF spectrum, channel length, wavelength, and receiver category.This work simulates the effects of varying parameters on the performance analysis and comparison of APD and PIN photo detectors using OWC channel at 1,550 nm wavelength. The purpose of using OWC channel is to transmit data signals to and from the under reliably over long distances. A comprehensive simulation analysis of APD and PIN photo detectors and their deployment in different applications are conducted.

II. THEORY AND PRINCIPLE

The Johnson (thermal) noise is assumed to be 4kTB, where k is the Boltzmann constant, T is the absolute photodiode temperature in Kelvin, B is the bandwidth of the system in Hertz, and R is the load resistor in Ohm. The net noise in APD photo detector is given by:

The shot noise is considered to be i2AYAL = i2thermal + i2av = 2e (Id) Bm2F , where e is the charge of an electron in coulomb , Iph is the photo - current Ib is the bulk current and Id is the dark current (nA). The net noise in PIN photo detector is given by :

$$i_{PIN}^2 = 2e\left(I_{ph} + I_B + I_D\right)B + \frac{4kTB}{R}, \quad (2)$$

where the shot noise is i2PIN = 2e (ID)B . Owing to the statistical nature of the avalanche progression, avalanche progression, avalanche photodiodes produce excess noise (F);

$$F = kM + (2 - \frac{1}{M})(1 - k), \qquad (3)$$

where excess noise factor (F) is a function of the carrier ionization ratio, k is expressed as the ratio of hole-to-electronionization probabilities (k < 1), and M is the multiplication gain.

III. SIMULATION DETAILS

The performance analysis and comparison of APD and PIN photodetectors using OWC channel is constructed. The simulation process is based on Optisystem software.The developed model consists of a transmitter, OWC channel, power splitter,and APD and PIN photodetectors.The optical signal is transmitted at a frequency of 193.4 THz and input power of 30 dBm. The proposed reference wavelength is 1,550 nm,which offers low attenuation and absorption losses.Besides, the transmitter has a linewidth of 10 MHz and extinction ratio of 20 dB.The simulation parameter settings for the optical transmitter are shown in Table 1. Subsequently, the optical input signal is sent through OWC channel of 300 km range.Power splitter is used to divide the path into two lines: one connected to APD and the other is connected to PIN photodetector.

After that, each photo detector is connected with low pass Bessel filter. The chosen simulation parameters for APD and PIN photo detector are shown in Table 2. Likewise, an eye diagram analyzer was utilized to measure the Q-factor and calculate the BER of the received signal. An electrical power meter visualizer is applied to measure the total power in dBm,whereas, oscilloscope visualizer is used to demonstrate the binary signal of NRZ pulses.

Parameters	Values
Reference wavelength (nm)	1,550
Power (dBm)	30
Extinction ratio	20
Linewidth	10
Modulation type	NRZ
Range of OWC channel (km)	300

Table 1. Simulation parameter settings for the optical transmitter

Parameters	Values	Values
Gain	3	-
Responsivity (A/W)	1	1
Ionization ratio	0.9	-
Dark current (nA)	10	10
Thermal noise	$1e^{-022}$	$1e^{-022}$
Shot noise (distribution)	Added (Gaussian)	Added (Gaussian)

Table 2. Simulation parameter settings for APD and PIN photodetector

IV. RESULTS AND DISCUSSION

A comparison model based on APD and PIN photodetectors is constructed with OWC channel with 300 km length and 1,550 nm wavelength. The constructed model is designed using OptiSystem 7.0 simulation software. The performance of the developed simulation design, which applies APD and PIN photodetectors using OWC channel,is investigated andevaluated in terms of output power, distance, and gain. The eye diagrams and gain (dB), signal output power (dBm),Q-factor, input power (dBm), extinction ratio (dB), thermal noise (w/Hz), and dark current (nA)are tabulated and tested for varying values of optical fiber length (km). A schematic of APD and PIN photodetectors setup using OWC channel designed for performances evaluation of the received signal at each photodetector. Figure 1 illustrates the main layout of APD and PIN photodetectors using OWC channel. Originally, the designed layout was simulated to investigate and analyze the performance between APD and PIN photodetectors using OWC channel. Thereafter, the input power is 30 dBm at the transmitter side and the OWC channel with range of up to 500 km. In order to investigate the performance of received signal, APD and PIN photodetectors are connected. An optical spectrum analyzer (OSA) and optical time domain are used to monitor the output signals after the OWC channel. Moreover, OSA is used as a tool to measure the optical power as a function of wavelength. The indicates that the proposed wavelength is at 1550 nm, as shown in Figure 2. Figure 3 shows the NRZ pulses of the transmitted signal, which are binary code.

The eye diagrams with minimum BER are shown in Figures 4 and 5. The eye diagram is clear and open, and the waveform distortion is substantially reduced with a high Q-factor of 257 at 1,550 nm wavelength for 300 km length, as presented in Figure 4.

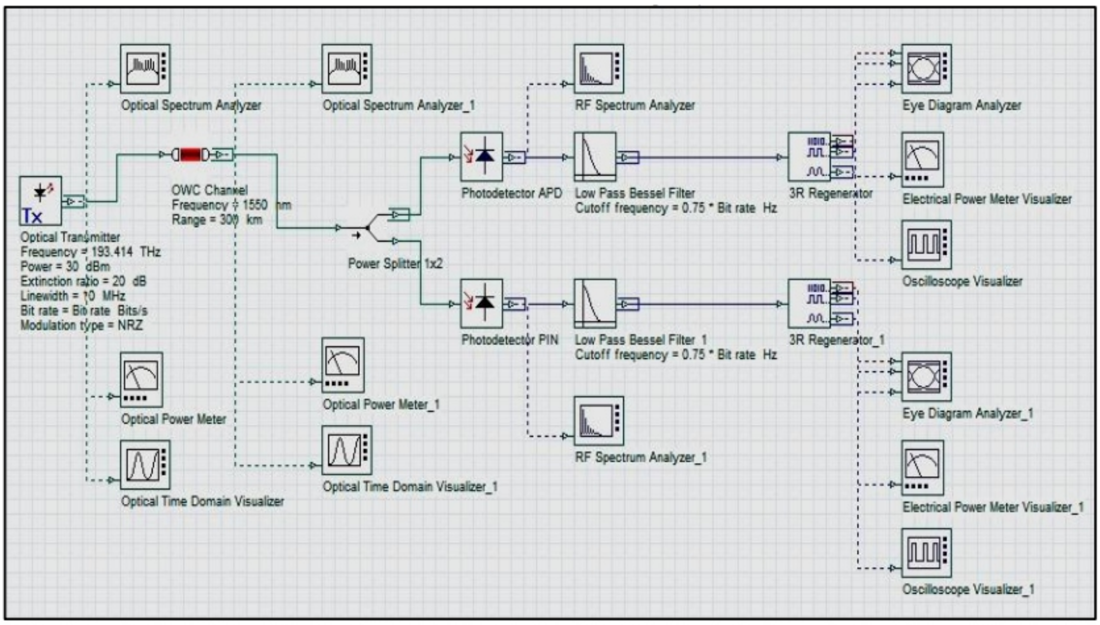

Figure 1: Designed model of APD and PIN photodetectors using OWC channel

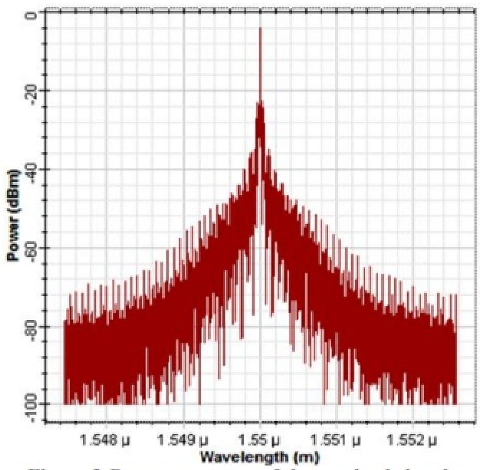

Figure 2:Power spectrum of the received signal.

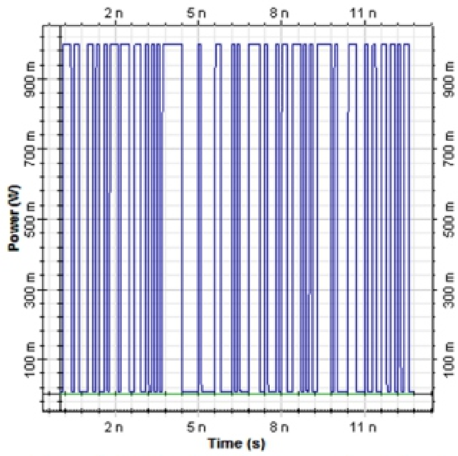

Figure 3: NRZ pulses of the transmitted signal

Eye diagrams are open and clear with attained low BER. This finding indicates improved performance of the system and corresponds to smallest signal distortion. Consequently, Figure 5 shows eye diagram with minimum BER for PIN photodetector with low Q-factor of 219 compared to APD photodetector. The red lines represent the curve of the minimum BER for the proposed design of APD and PIN photodetector.

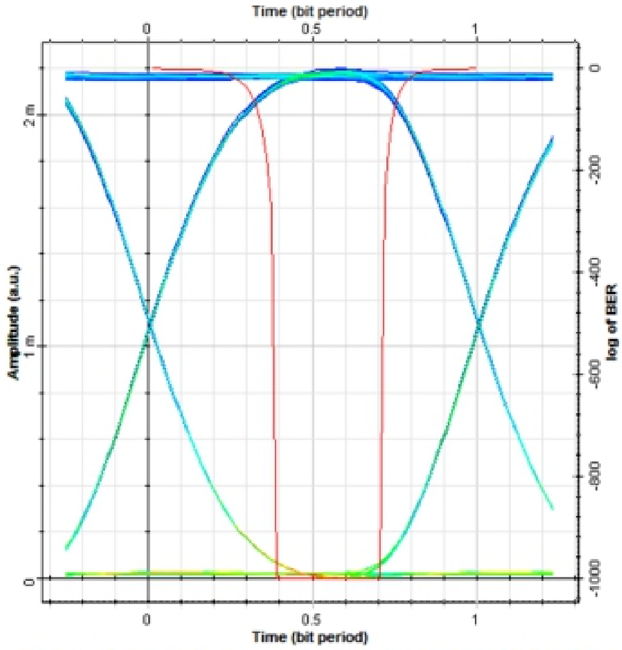

Figure 4: Eye diagram with minimum BER of APD photodetector

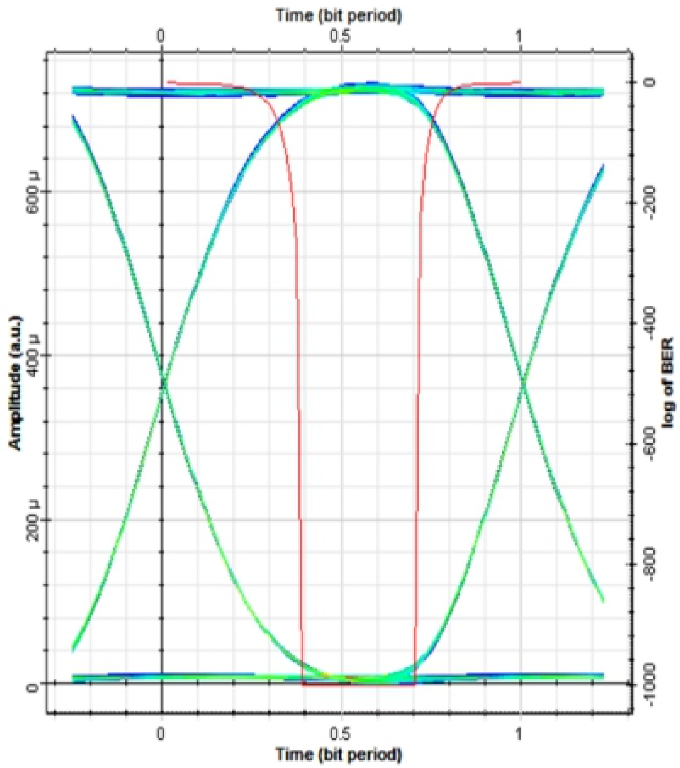

Figure 5: Eye diagram with minimum BER of PIN photodetector

Figure 6 shows the signal output of the APD photodetector in binary form, which is represented in amplitude with respect to time. Figure 7 shows the signal output when PIN photodetector is implemented. The Oscilloscope visualizer shows a clear code without any distortion or noise compared to the code represented in Figure 7. Moreover, as revealed in Figure 6, the implementation of APD photodetector shows high amplitude of the signal compared to the implementation of PIN photodetector as shown in Figure 7.

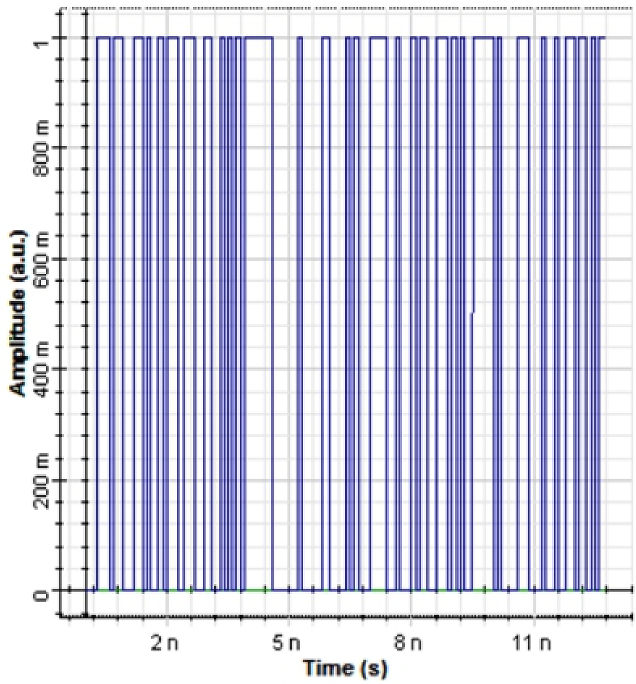

Figure 6: Code output of APD photodetector

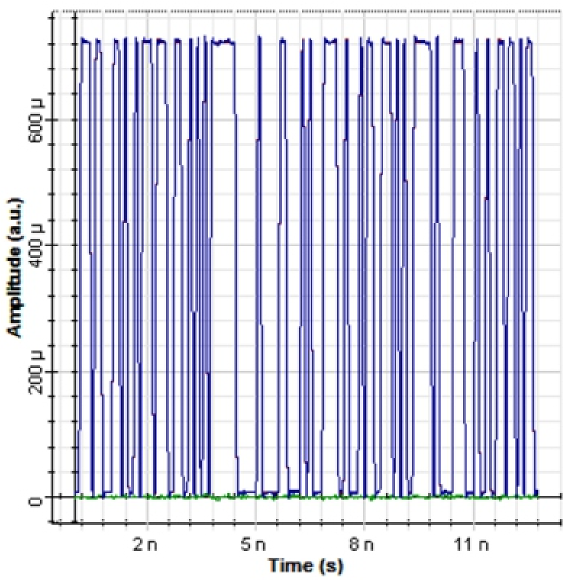

Figure 7: Code output of PIN photodetector

RF spectrum analyzer is a test instrument utilized to provide an effective insight into the RF performance of signal. RF spectrum analyzer characterizes the frequency domain, noise, and distortion by comparing the input and output spectra in order to compare between APD and PIN photodetector performance. Figures 8 and 9 show the RF spectrum of the proposed model for both APD and PIN photodetector, respectively. The RF signal of APD photodetector over a range of frequency reveals a highly sensitive power detector and large bandwidth as shown in Figure 8. Furthermore, the RF signal of PIN photodetector demonstrates a low sensitive power as shown in Figure 9 compared with thatin Figure 8.

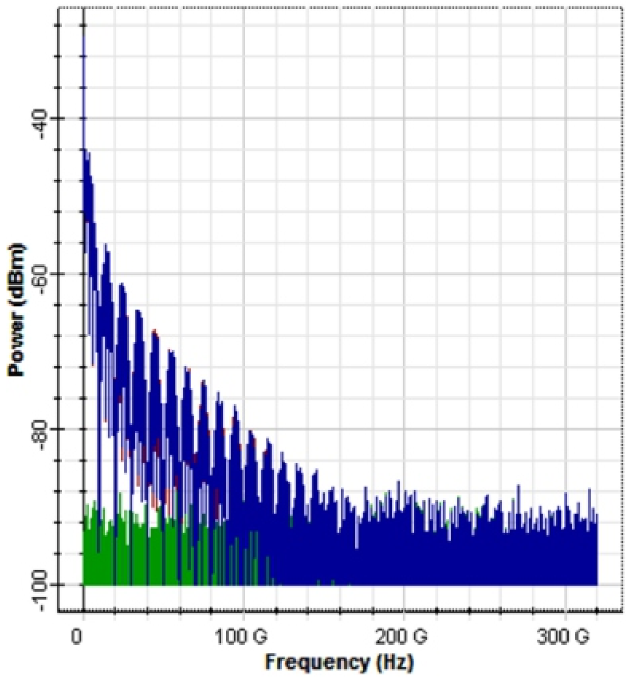

Figure 8: RF spectrum of APD photodetector

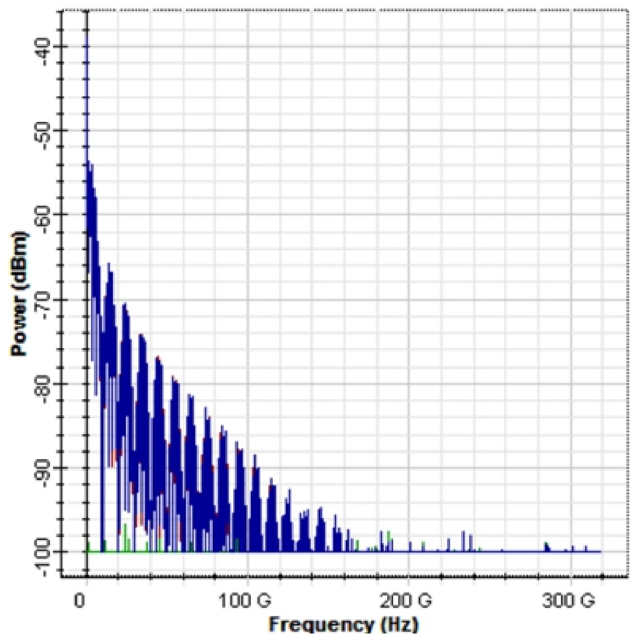

Figure 9: RF spectrum of PIN photodetector

Table 3 displays the results of the output readings different OWC channel range values. The Q-factor values are decreased as the OWC channel range increases for APD and PIN photodetector. Furthermore, small values are observed in the electrical power and the optical power of the received signal via APD photodetector. By contrast, the Q factor value of PIN photodetector is lower than APD photodetector at 300 km as shown in Table 3. Together, the electrical power of the captured signal by PIN photodetector is 36.35 which leads to unstable system performance.

Furthermore, this study simulates a new developed model based on OWC channel using APD and PIN photodetector, and compares with those of O. Kharraz et al. [1] andH. Hamadouche et al. [2]. From the comparison, the current study shows high and stable performances of the received signal using APD photodetector with zero-bit error rate (BER) over a distance range of 300 km along the communication system.

Range (km)	Q-factor of APD	Q-factor of PIN	Electrical power of APD (dBm)	Electrical power of PIN (dBm)	Optical power at Tx (dBm)	Optical power at Rx (dBm)
100	763.2	954.3	−7.73	−17.27	26.97	8.11
200	401	411.7	−19.77	−29.31	26.97	2.1
300	257.2	219.5	−26.81	−36.35	26.97	−1.43
400	182.2	135.6	−31.81	−41.35	26.97	−3.94
500	137.1	91.19	−35.69	−45.23	26.97	−5.88

Table 3: Output results by varying the OWC channel distance

Table 3 shows that the proposed model presents several advantages of using APD photodetector in terms of Q-Factor, electrical output power signal, optical output power signal, and BER. In general, the simulation design of APD photodetector is characterized by an excellent Q-Factor of 257.2, electrical output power signal of 26.81, and optical output power signal of 1.43. The developed design of APD photodetector shows clear eye diagram with 257.2 Q-factor compared with 7 and 14.5 in O. Kharraz et al. [1] andH. Hamadouche et al. [2], respectively.

Figure 10 presents the receiver sensitivity versus the extinction ratio of the transmitter for APD photodetector based OWC channel. In fact, the sensitivity is degraded at APD receiver output as the extinction ratio increased with APD gain of 3.In brief, the proposed design shows high receiver sensitivity of 26.647 dBm compared with that of O. Kharraz et al. [1], which is 31.1 dBm.

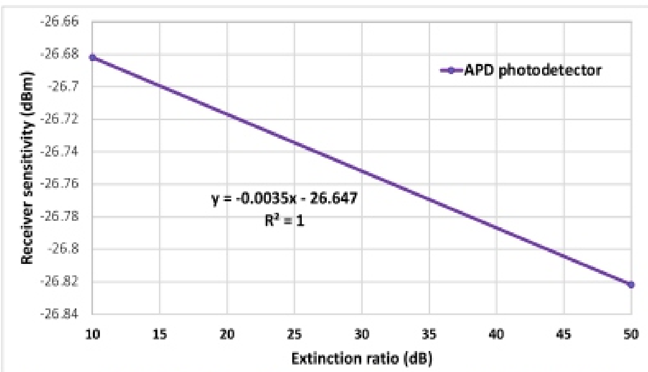

Figure 10: Extinction ratio vs. receiver sensitivity for APD photodetector

Thermal noise in the APD and PIN photodetector affects their Q-factor values. Figure 11(a) shows that as the thermal noise increases, both Q-factor values decrease. At the same time, as predicted in Figure 11(b), APD photodetector is more affected than PINwhen the dark current is high; therefore, the shot noise dominates on the system.

Significantly, the dark current of Germanium photodetectors is normally around the value of 85000 nA to bepractical. Consequently, the cross-over point in this case is around 83500 nA, as shown in Figure 11(b).

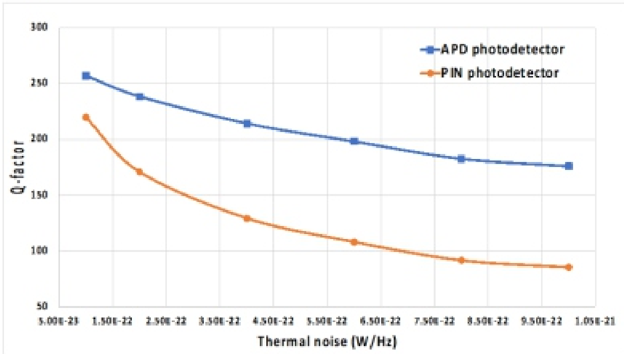

(a)

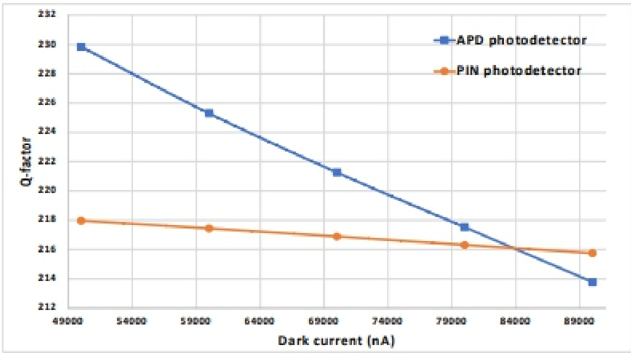

(b)

Figure 11: Outputs values of APD and PIN photodetector in terms of (a) Thermal noise vs Q factor and (b) Dark current vs Q-factor

IV. CONCLUSION

In the present study, a performance analysis and comparison of APD and PIN photodetectors receivers using OWC channel is investigated in detail. APD photodetector is more appropriate for long-haul communication distance, which results in high signalto-noise ratio because of the large bandwidth and the internal gain. On the one hand, the internal gain of APD photodetector is its great advantage over the PIN photodetector.

This gain assists in revoking other generated noise in the system. Besides, APD photodetector is a flawless candidate in highly sensitive optical-electrical communication applications. However, APD photodetector fails to be superior over PIN when shot noise is high. On the other hand, PIN photodetector is simpler, inexpensive to manufacture, and highly reliable for short-distance and low-bandwidth application compared to APD photodetector. Furthermore, PIN photodetector is insensitive to dark current because it has many layers; thus, the depletion region is smaller than that of the APD photodetector.

ACKNOWLEDGMENT
The author would like to thank Palestine Technical University–Kadoorie (PTUK) for supporting and funding this research.

REFERENCE

[1] Kharraz O., Forsyth D., "Performance comparisons between PIN and APD photodetectors for use in optical communication systems". Optik, 1;124(13), pp.1493-1498, Jul 2013. DOI: http://dx.doi.org/10.1016/j.ijleo.2012.04.008.

[2] Hamadouche H., Boualem M., Mouweffeq B., "Performance comparison of APD and PIN photodiodes using RZ and NRZ". Process. Pattern Recognit, 9, pp. 4257-64. 2016. DOI:https://www.researchgate.net/publication/343214296.

[3] Singh M., Arora S., and Rajveer, "Performance Comparison between PIN and APD Photodiodes for use in Free Space Optical Communication Link". International Journal of Innovative Research in Advanced Engineering (IJIRAE), 8 (2), pp. 25-28, August 2015. DOI:https://www.ijirae.com.

[4] FASSI B., DRIZ S., and METIOUI C., "APD Photodiode Impact on ZCZ Optical CDMA Performance". The International Conference on Materials Science andEngineering and Their Impact on The Environment 26-28, University of Djillali Liabes, Sidi Bel Abbes 22000, Algeria, 28 Novembre 2019. DOI:https://scholar.google.com/citations.

[5] Shabaneh, A.A., 2020. "Investigative Modeling of Symmetric Fiber Bragg Grating as Dispersion Compensation for Optical Transmission System". Optica pura y aplicada, 53(4), p.7. 2020. DOI:10.7149/OPA.53.4.51052.

ISSN Print : 2320-2084, Online : 2321-2950

IMAGE DEHAZING USING AIR LIGHT ESTIMATION AND MODIFIED IDERS MODEL

JAVEED MD, B. BHARATHI, K. NARESH
Associate Professor, Department of Electronics and Communication Engineering, SreeDattha Institute of Engineering and Science, Hyderabad, Telangana, India

ABSTRACT

Images captured in hazy conditions, such as haze, fog, thin cloud, snow, silt, dust, off gas, etc., suffer from severe colour and contrast degradations. This includes remote sensing images (RSIs) as well as any other images captured in these conditions. As a result, there is a significant demand for dehazing algorithm to restore hazed RSIs from their degradations. The vast majority of dehazing algorithms that can be found in published works were initially developed for natural images dehazing (NID). In the context of our investigation, the physical model of NID is distinct from that of RSI dehazing (RSID), which has not been thoroughly discussed up until this point. In this paper, a novel idea referred to as "virtual depth" in relation to the physical model of RSI is presented for the first time. Real depth in a nature image is measured by the coverings of the earth's surface, such as snow, dust, cloud, and haze or fog. Virtual depth, on the other hand, gives the distance of an object departing from the foreground, whereas real depth measures the distance of an object departing from the foreground. These coverings serve the same purpose as the hazes in a natural photograph, namely to provide a hint of foreground and background. Dehazing operator is implemented iteratively to remove haze progressively until arriving at a result that is satisfactory in the second method, which is referred to as Iterative Dehazing for Remote Sensing image (IDeRS), which is proposed. In IDeRS, we also develop a fusion model for combining patch-wise and pixel-wise dehazing operators in order to eliminate halos and the oversaturation that is caused by them, respectively. This model is used to combine the two types of dehazing operators. The proposed IDeRS outperforms the majority of the state-of-the-art techniques in RSID, as shown by extensive experimental results tested on databases that are accessible to the general public.

Keywords- Dehazing, MATLAB, High resolution images, Natural image, IDERS, Air light Estimation.

I. INTRODUCTION

The very high resolution (VHR) satellite (such as IKONOS, SPOT5, Quickbird-2, Worldview 2, GeoEye-1 and Pleiades-1A) and aerial images have been providing remote sensing images (RSIs) with an increasing high spatial resolution, stable geometric location, and detailed textural information as remote sensing technology has advanced. Scene-level geographic image classification [1] and geospatial object detection [2] are two fundamental research topics that have garnered a lot of attention recently. [1] and [2] However, due to contrast degradation and colour attenuation, these two tasks, which include image analysis and search [3, 4], frequently suffer from poor quality optical RSIs. There are two primary factors that contribute to the low quality of RSIs. To begin, the quality of the RSI is typically susceptible to unfavourable atmospheric conditions, such as the appearance of haze, fog, smoke, and clouds, amongst other things. This is because the optical remote sensors that are carried aboard satellites and aircraft capture electromagnetic signals that are located far from the surface of the earth through the atmosphere layer. In addition, even on days with no clouds or precipitation, the atmosphere cannot be completely devoid of any particle; consequently, haze is always present, which contributes to the poor visibility. Second, the surface reflectance coefficients or surface albedos of various objects, including those that have been created by humans as well as land-use/landcover (LULC) parcels, are not the same. Even for the same object, the wide-field of VHR RSI can cause it to be covered by heterogeneous translucent coveringcontaminations. This can happen even for the same object. "hazes" of RSI are those translucent coveringcontaminations covering on the earth's surface, such as haze/fog, thin could, snow, silt, dust, offgas, and other such things. This is because of the two reasons that were mentioned above. Research into RSI enhancement, which includes methods such as histogram equalisation [5], homographic filter, and Retinex theory [6], has been conducted in depth. The goal of this research is to improve the RSI's overall quality. However, because this improvement did not take into account the physical mechanism that causes haze, it is unable to remove haze effectively and, as a result, suffers from artefacts such as oversaturation and gradient reversal. In point of fact, the optical distances between the objects in the scene and the sensor for RSIs cause haze to increase at an exponential rate. As a result, it is of the utmost importance to investigate the physical mechanisms that cause haze in order to develop models for RSI dehazing (RSID) [7, 8]. When it comes to NID, the physical model of haze [9] has been well received. For effective dehazing, precise estimations of atmospheric light and transmission map are required. At a minimum, there are three key distinctions to be made between the RSID and the physical models of natural image dehazing (NID). The natural image is first captured by the camera, which is typically aimed in a direction that is further away from the subject. As the scene depth increases, the image's contrast and colour saturation become increasingly less appealing. This property makes a number of prior contributions [10-15] toward the process of deriving the transmission map for NID. However, RSI is typically gathered by remote optical sensors aboard satellites, which are located a great distance from the earth; as a result, the scene depth that it provides is relatively consistent. Second, the estimation of atmospheric light, with very few exceptions, is typically done in a haphazard manner [16] or is decided by the pixel with the most hazeopacity [17]. When referring to natural images, the haze-opaque region almost always refers to the sky region. On the other hand, an RSI almost never contains any sort of sky region. Third, remote sensing images (RSIs) are typically captured with a diverse range of spatial resolution (typically between 0.2 metres and 30 metres), scale, and shape of the objects on the earth's surface, whereas natural images typically have a resolution and scale that are comparable to one another. As a result, the hazes typically have a diverse collection of RSIs. Therefore, NID methods that were developed for a straightforward scenario are unable to effectively remove the hazes caused by RSIs. The application of an NID to RSID is hindered in its effectiveness as a result of these three distinctions. Even though some NID models have been used to study RSID [18], there are three key differences between the two that need to be carefully considered in order to realise their full potential. In more recent times, learning-based dehazing has been the subject of extensive development [19-23]. It learns from a database of image pairs consisting of clear images and hazy images to train itself. To generate hazy images for the database, computer models are used. These models require accurate scene depth measurement, which is currently not possible for outdoor scenes, including RSIs. Nonetheless, hazy images are generated from the database. Taking into account the three distinctions, our proposal is an iterative dehazing model for remote sensing images (IDeRS). To begin, the haze-line prior [24] rather than the haze-opaque pixel is utilised in the process of computing the atmospheric light of an RSI. The latter has seen widespread application for the treatment of NID. On the other hand, it is not present in the vast majority of RSIs. Second, even though the natural image hazes and RSI hazes are caused by different things, the transmission maps of both of these types of hazes can be expressed using the same mathematical formulas. In point of fact, each of them is proportional in an exponential fashion to the "optical depth" of the scenes contained within an image. It suggests that the transmission map model of natural image can also be applied to RSI, albeit with a different way of interpreting its results. Third, an iterative framework is proposed for the progressive elimination of the haze. The iterative procedure is particularly well-suited for RSID due to the fact that it can eliminate haze on a number of different scales in a step-by-step manner. IDeRS was developed with the dark channel prior (DCP) dehazing [25] as its foundation. This dehazing method was well received, particularly for NID. It is also common knowledge that after dehazing, DCP images have surprisingly fewer saturated pixels (pixels that are either completely black or completely white). This is beneficial for the interpretation of RSI in a variety of applications involving object detection, recognition, and other similar tasks. The DCP, on the other hand, was developed for only one scale, so it would be unable to remove haze at various scales for RSIs, which would result in significant halo artefacts. As a result, the iterative approach is suggested throughout the course of this work. Additionally, the final condition of the iterative process to arrive at an adaptive IDeRS for a variety of scenarios is presented here.

Extensive research was done on the dehazing of single images [26] and [27]. Single image dehazing refers to the situation in which there is only one hazy image that can be dehazed, which is a classic example of an ill-posed problem. The extraction of depth data or the estimation of transmission maps is necessary for successful dehazing. Numerous priors, such as DCP [28], Bayesian statistical prior [29], color-line prior [30], colour attenuation prior [31], haze-line prior [32], difference-structure-preservation prior [33] and colour ellipsoid prior [34], have been proposed in an effort to solve the ill-posed problem of dehazing. When applied to a single natural image, these priors produce a depth/transmission map with a high degree of accuracy. In determining the raw transmission map, Meng et al. [35] extend the concept of DCP [36] by introducing its lower bound. After that, they introduce an L1-norm based contextual regularisation in order to suppress halo artefacts. Zhu et al. [37] create a linear model under a colour attenuation prior in order to recover the depth of the scene. This means that the depth of the scene has a positive correlation with the difference between lightness and saturation. Berman et al. [38] propose a nonlocal method in which the transmission map and atmospheric light estimated across the entire image rather than in local patches based on the haze-line prior. In this method, the haze-line prior is not used. Recent years have seen the development of a number of deep learning–based dehazings, such as DHNet [39], MS-CNN [40], AOD-Net [41], and Ranking-CNN [42]. They directly learn transmission maps based on the databases that are provided to them. These databases are made up of paired colour images of interior spaces along with the ground-truth depths of those spaces. Cai et al. [43] present an end-to-end CNN system that they call DehazeNet. It is made up of four layers, which are as follows: a layer for feature extraction, a layer for multi-scale mapping, a layer for local extremum, and a layer for nonlinear regression that uses the BReLU activation function. The authors Ren et al. [44] propose using a multi-scale CNN to estimate the transmission map. This CNN has two different networks: one at a coarse scale and one at a finescale. More and more of the most recent NID research has been centred on training models with Generative Adversarial Networks (GAN) [45] or Conditional GAN [46], such as cGAN-Dehaze [47] and DCPDN [48]. [45] & [46] The majority of research focuses on natural dehazing techniques for images. Although some models of NID have been successfully applied to RSID [49], the difference between NID and RSID ought to be well addressed for the purpose of achieving the best possible performance. In the case of RSID, earlier methodologies were primarily intended to improve the contrast of hazy RSI. Richter [50] eradicated the haze by creating transition regions that were seamlessly haze-free and haze-free. In order to characterise land cover, Du et al. [51] developed a wavelet transform analysis (HAWAT) technique by making use of the haze-free reference image of the same area. Under the stipulation that the blue and red bands are highly correlated, Zhang et al. [52] proposed a haze optimised transformation (HOT) as a method to detect and remove haze from an image. Based on the HOT algorithm, Moro and Halounova [53] presented a framework that could successfully remove haze from IKNOS imageries. This framework was presented in their paper. A background suppressed haze thickness index (BSHTI) was developed by Liu et al. [54] for the purpose of removing spatially varying haze contamination. This index is comprised of three steps, and they are as follows: haze detection, haze perfection, and haze removal.

II. ITERATIVE DEHAZING METHOD

The currently available model is unable to clear the haze from the natural images, and its accuracy decreases to an unacceptable level as noise levels rise. A fresh methodological approach, as depicted in Figure 1, has been suggested as a solution to these issues.

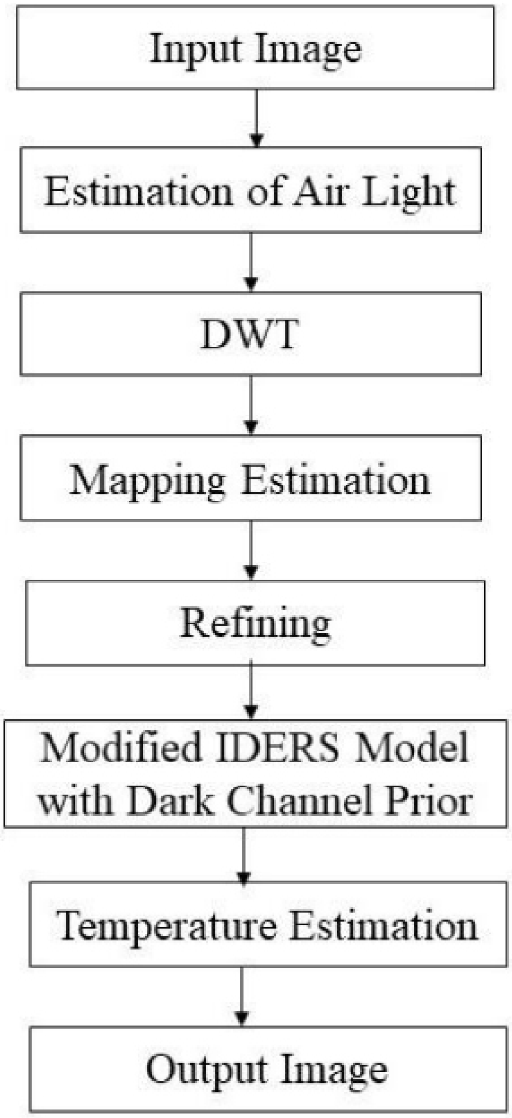

Fig 1. Dehazing using MIDERS

A. ESTIMATE AIR LIGHT

The weather is cloudy, sunlight, denoted by S, is disregarded, and only the atmospheric light, denoted by A, is taken into consideration, then the brightest pixels in the hazy image are thought to be the most haze-opaque. However, this is only the case if the weather is cloudy.

Estimate air light is the primary component of the DCP that is utilised in the process of improving satellite image qualities through the application of remote sensing image processing. Estimating the values of the air light for use in the generation of the transmission matrix is the primary goal of this section. The first thing that is done is to convert the colour image into three-indexes such as red, green, and blue. The next step is to extract the low intensity pixels; the number of clusters in satellite images will be higher, while the opposite will be true for normal images. After that, the clusters need to be reorganised for the fresh estimation of the transmission map. These clusters will be separated into three different groups or colour channels according to the air light values that are present (RG, GB, and RB). After that, new values for the air light will be generated based on the updating of the previous values for the air light, as shown in figure 2.

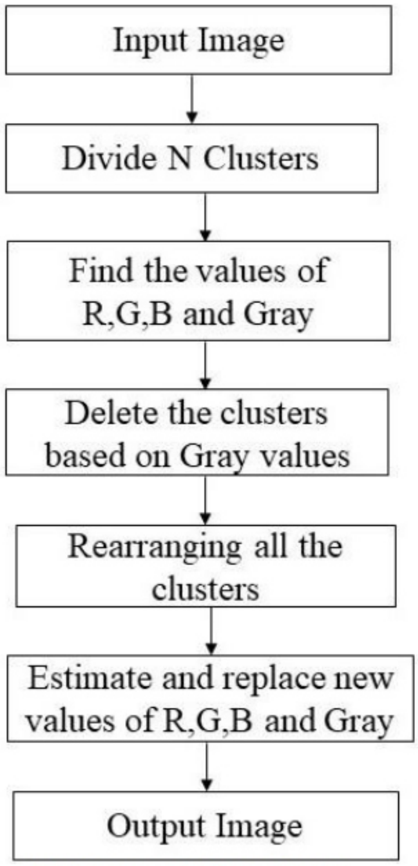

Fig 2. Process of estimate air light

B. MAP ESTIMATION

Estimation of atmospheric light takes place, then transmission is estimated as follows:

$$f(x) = 1 - \omega \min_{y\epsilon\Omega(x)} \left(\min_{e} C \left(\frac{I^C(y)}{A^C_\infty} \right) \right)$$

The amount of haze that is intentionally left in the image to prevent unnatural scenes (= 0.95)In order to improve the quality of the transmission map, soft matting Laplacian is applied to the edges in order to smooth out any artefacts. However, this results in a significant increase in the amount of time required for computation.

It is dependent on the assumption that, for any given pixel in a shading picture of a typical scene, one channel (either red, green, or blue) is typically dark, with the exception of the sky. These dark pixels will typically be illuminated by the air light, and as a result, the evaluation of this light source begins with the pixels that are the darkest in the scene. [6] is the source of the motivation for this perception, which is also known as the dark channel prior. The value for the dark channel, J dark(x), can be calculated using the hazy picture, J(x).

$$J^{dark}(x) = \min_{c\in(y,g,b_1)} \left(\min_{y\in\Omega(x)} \left(j^c(y) \right) \right)$$

Jc is a shading channel of J, and a local patch focused at x is denoted by the notation (x). In [7], dark channels are processed utilising a patch size 15×15. There are not many insights provided to characterise the patch size; however, the probability that the patch contains dark pixels increases in proportion to the patch's growing size. The accuracy of the evaluation of the dark channel could then be achieved. In any case, when dealing with a large patch, the presumption that the transmission is consistent within a patch is shown to be less accurate, and the number of hollow artefacts that occur close to depth edges grows. The majority of DCP-based DE hazing strategies calculate the dark channel by essentially making use of a local patch that is a fixed size in order to fundamentally reduce the amount time spent computing. A number of the DCP-based alignment strategies consider a patch with a size different from 15 by 15, which was the standard configuration. The size of the patch can be adjusted progressively, taking into account the contents of the picture. Some of them reduced the amount of work that required a lot of time by using a patch size of 11 by 11 [8]. When a small patch size is used in the initial cloudy picture that also includes limited light, real-world over-satiation effects can occur in the recovered scene's radiance. This results in a sense of disillusionment regarding the recognisable evidence of the environmental light source. Increasing the size of the image can help fix this problem, but it can also cause halo effects and black artefacts, especially along the edges. In this manner, two patch sizes, 3x3 and 45x45, have been utilised in a procedure of DCP. Both of these patch sizes have been provisionally recognised.

An inaccurate estimation of the transmission map could result in a few mutilations, such as the destruction of square antiquities. A cloudy transmission map is the result of using a patch-based dark channel figuring method. The fundamental reason for this is the assumption that there is a constant incentive present in a particular area patch. This is not always the case, particularly when the patch in question has a pointed edge. The obvious edge artefacts that result from this incorrect assumption are as follows: A number of approaches have been tried out in the interest of producing a more accurate map

In several different DE hazing methods, the map is given a smoother appearance with the assistance of the Gaussian filter. Some other people have used rather than the bilateral filter, which is fundamentally the same as Gaussian convolution, but pixels are handled based on nearby area and comparative qualities rather than bilaterally. A smoothing channel that also protects the edges is called a Gaussian filter. The Guided filter, which is similar to the bilateral filter, performs edge safeguarding. However, its activity is at its peak in the vicinity of the edges. The developers of this method decided to replace the soft matting that was used in the first DCP strategy with a guided filter so that the transmission refinement map could be completed much more quickly. This was done because the use of soft matting was extremely time consuming. As a direct consequence of this, the soft matting has never been utilised in any other method of DE hazing in the future. On the other hand, the guided filter has been implemented subsequently in a variety of different strategies.

The primary difference between these refinement calculations and others is that, unlike the Gaussian and the Bilateral filters, the soft matting, the Cross-two-sided filter, and the Guided filter take into consideration the grey image as well as the colour hazy image of the transmission map. This is the fundamental contrast point. This helps in removing the incorrect surfaces that are dependent on the real colours and maintaining a level of sharpness that is comparable to the initial colour hazy picture.These valid calculations have been applied to the transmission map in order to improve it. However, other calculations apply a pre-preparing upgrading calculation to the hazy picture in order to prevent the transmission map from having surfaces that are obscured and incorrect

.

C. GET RADIANS

This step will identify whether the light temperature of the image has been increased or decreased when compared with the original image in preparation for subsequent enhancement operations.

D. LIME

When either the light exposure or lime concept is utilised, the light levels will be adjusted on their own automatically. Only the middle value of the image is considered, and after that, it is modified so that it only affects the parts of the image that contain the middle value.

The simulations are run on natural image datasets as well as satellite image datasets, and they are implemented on mat lab software in order to get the results that are presented here.

(a) Input image 1 (b) DCP process output 1 (C) DE hazed output 1

(a) Input image 2 (b) DCP process output 2 (C) DE hazed output 2

(a) Input image 3 (b) DCP process output 3 (C) DE hazed output 3

(a) Input image 4 (b) DCP process output 4 (C) DE hazed output

Parameters	Image 1	Image 2	Image 3	Image 4
PSNR	11.45	35.89	19.34	17.6
SSIM	0.67	0.82	0.73	0.91
MSE	34.46	11.36	24.36	26.32
ACCURACY	98.2%	99.1%	99.2%	98.9%
TIME (Secs)	1.21	1.08	1.04	0.13

Table 1: Summary of Parameters

III. CONCLUSION

An iterative dehazing method for single RSI, which will be referred to as IDeRS, will be proposed in this article. In the first step of this research, we investigate the viability of various dehazing algorithms and general haze optical models applicable to the RSID. In terms of its optical model, the RSID is distinct from the NID in that it possesses almost constant depth and does not contain haze opaque pixel. Additionally, the haze-opaque pixel is absent. The estimation of the transmission map and the estimation of the atmospheric light would both be invalidated as a consequence of these two differences. In order to solve the first issue, we came up with the concept of "virtual depth," which is essentially the same thing as the natural image's actual depth but measures the amount of covering and contamination on the earth's surface. The second issue can be remedied by making use of the haze-line prior in place of the haze-opaque pixel in order to solve the problem. Second, a fusion model that combines pixelwise and patch-wise transmission map estimations has been proposed as a solution to the problems of over-saturation and halo that are caused, respectively, by pixel-wise and patch-wise dehazings. This is done in order to overcome the problems. Thirdly, in order to implement transmission map estimation and the overall process of dehazing, an iterative procedure is developed. Last but not least, evaluations on a wide variety of RSIs downloaded from the NASA Earth Observatory website as well as five well-known databases demonstrate that the proposed IDeRS is able to better recover high quality images by gradually removing halo artefacts during the iterative process while simultaneously suppressing oversaturation. This is done in order to improve image recovery. Patch segmentation fusion is going to be the primary focus of our future work. First, an image is cut up into many smaller patches, and then the segmentation process is carried out on each individual patch. In this case, the sharpening method is used to round off the image's edges in order to improve the underwater image's visibility over a wider range. Patch segmentation will be the primary focus of our future work.

REFERENCE

[1] Alajarmeh A, Zaidan A (2018) A real-time framework for video Dehazing using bounded transmission and controlled Gaussian filter. Multimed Tools Appl 77(20):26315–26350. https://doi.org/10.1007/s11042-018-5861-4

[2] 2Ancuti CO, Ancuti C (2013) Single image Dehazing by multi-scale fusion. IEEE Trans Image Process 22(8):3271–3282. https://doi.org/10.1109/TIP.2013.2262284

[3] Cai B, Xu X, Jia K, Qing C, Tao D (2016) DehazeNet: an end-to-end system for single image haze removal. IEEE Trans Image Process 25(11):5187–5198. https://doi.org/10.1109/TIP.2016.2598681

[4] Cheng F-C, Cheng C-C, Lin P-H, Huang S-C (2015) A hierarchical Airlight estimation method for image fog removal. EngApplArtifIntell 43:27–34. https://doi.org/10.1016/j.engappai.2015.03.011

[5] Cooper TJ, Baqai FA (2004) Analysis and extensions of the Frankle-McCann Retinex algorithm. J Electron Imag 13(1):85–92. https://doi.org/10.1117/1.1636182

[6] Dippel S, Stahl M, Wiemker R, Blaffert T (2002) Multiscale contrast enhancement for radiographies: Laplacian pyramid versus fast wavelet transform. IEEE Trans Med Imag 21(4):343–353. https://doi.org/10.1109/tmi.2002.1000258

[7] X Dong, X Hu, S Peng, and D Wang (2010). Single color image dehazing using sparse priors," IEEE Int.Conf. Image Process., Hong Kong, China, pp. 3593–3596, 2010

[8] Fattal R (2008) Single Image Dehazing. ACM Trans Graph (TOG) 27(3):1–9. https://doi.org/10.1145/1360612.1360671

[9] Fattal R (2014) Dehazing using color-lines. ACM Trans Graph 34(1):1–14. https://doi.org/10.1145/2651362

[10] KB Gibson and TQ Nguyen (2013), "Fast single image fog removal using the adaptive wiener filter," IEEEInt. Conf.Image Process., Melbourne, VIC, Australia, pp. 714–718, 2013[11] N Hautiere, J Tarel, and D Aubert (2007). "Towards fog-free in-vehicle vision systems through contrastrestoration," IEEE Conf. Comput. Vision Pattern Recognition, Minneapolis, MN, USA, pp. 1–8, 2007

[12] He K, Sun J, Tang X (2011) Single image haze removal using Dark Channel prior. IEEE Trans Pattern AnalMach Intell 33(12):2341–2353. https://doi.org/10.1109/TPAMI.2010.168

[13] He K, Sun J, Tang X (2013) Guided image filtering. IEEE Trans Pattern Anal Mach Intell 35:1397–1409. https://doi.org/10.1109/TPAMI.2012.213

[14] Huang S, Chen B, Wang W (2014) Visibility restoration of single hazy images captured in real-worldweather conditions. IEEE Trans Circuits Syst Video Technol 24(10):1814–1824. https://doi.org/10.1109/TCSVT.2014.2317854

[15] Jessica E, Steven L, Jean-Baptiste T (2018) Color and sharpness assessment of single image Dehazing.Multimed. Tools Appl 77(12):15409–15430. https://doi.org/10.1007/s11042-017-5122-y

[16] Jiang B, Meng H, Ma X, Wang L, Zhou Y, Xu P, Jiang S, Meng X (2018) Nighttime image Dehazing withmodified models of color transfer and guided image filter. Multimed Tools Appl 77(3):3125–3141. https://doi.org/10.1007/s11042-017-4954-9

[17] Kim J-H, Jang W-D, Sim J-Y, Kim C-S (2013) Optimized contrast enhancement for real-time image andvideo Dehazing. J Vis Commun Image Represent 24(3):410–425. https://doi.org/10.1016/j.jvcir.2013.02.004

[18] Kim TK, Paik JK, Kang BS (1998) Contrast enhancement system using spatially adaptive histogramequalization with temporal filtering. IEEE Trans Consum Electron 44(1):82–87. https://doi.org/10.1109/30.663733

[19] Kopf J, Neubert B, Chen B, Cohen M, Cohen-Or D, Deussen O, Uyttendaele M, Lischinski D (2008) Deep Photo: Model Based Photograph Enhancement and Viewing. ACM Trans. Graph. (TOG) 27(5):116. https://doi.org/10.1145/1409060.1409069

[20] L Kratz and K Nishino (2009). "Factorizing scene albedo and depth from a single foggy image," IEEETwelth Int. Conf. Comput. Vision, Kyoto, Japan, pp. 1701–1708, 2009

[21] Lee J, Li C, Lee H (2019) Visibility Dehazing based on channel-weighted analysis and illumination tuning.Multimed Tools Appl 78(2):1831–1856. https://doi.org/10.1007/s11042-018-6280-2

[22] Li QH, Bi DY, Xu YL, Zha YF (2014) Haze Degraded Image Scene Rendition. Acta AutomSinica 40:744–https://doi.org/10.3724/SP.J.1004.2014.00744

[23] Li Z, Zheng J, Zhu Z, Yao W, Wu S (2015) Weighted guided image filtering. IEEE Trans Image Process24(1):120–129. https://doi.org/10.1109/TIP.2014.2371234

[24] Lu H, Li Y, Nakashima S, Serikawa S (2016) Single image Dehazing through improved tmospheric lightestimation. Multimed Tools Appl 75(24):17081–17096. https://doi.org/10.1007/s11042-015-2977-7

[25] G Meng, Y Wang, J Duan, S Xiang, and C Pan (2013), "Efficient image dehazing with boundary constraintand contextual regularization," IEEE Int. Conf. Comput. Vision, Sydney, NSW, Australia, pp. 617–624,2013.

[26] SG Narasimhan and SK Nayar (2003). "Interactive (de) weathering of an image using physical models,"IEEE Int. Conf. Comput. Vision Workshop Color Photometric Methods Comput. Vision, New York, NY,pp. 1–7

[27] Narasimhan SG, Nayar SK (2003) Contrast restoration of weather degraded images. IEEE Trans PatternAnal Mach Intell 25(6):713–724. https://doi.org/10.1109/TPAMI.2003.1201821

[28] SK Nayar and SG Narasimhan (1999). "Vision in Bad Weather," Proc. Seventh IEEE Int. Conf. Comput.Vision, Kerkyra, Greece, pp. 820–827

[29] Nishino K, Kratz L, Lombardi S (2012) Bayesian Defogging. Int J Comput Vis 98(3):263–278. https://doi.org/10.1007/s11263-011-0508-1

[30] H Park, D Park, DK Han, and H Ko (2014). "Single image haze removal using novel estimation ofatmospheric light and transmission," IEEE Int. Conf. Image Process. (ICIP), Paris, France, pp. 4502–4506,2014.

[31] M Pedone and J Heikkilä (2011). "Robust airlight estimation for haze removal from a single image," IEEEComput. Vision Pattern Recognition Workshops, Colorado Springs, CO, USA, pp. 90–96

[32] YY Schechner, SG Narasimhan, and SK Nayar (2001). "Instant dehazing of images using polarization,"IEEE Conf. Comput. Vision Pattern Recognition, Kauai, HI, USA, pp. 325–332

[33] Seow M-J, Asari VK (2006) Ratio rule and Homomorphic filter for enhancement of digital colour image.Neurocomputing 69(7):954–958. https://doi.org/10.1016/j.neucom.2005.07.003

[34] Shiau Y, Yang H, Chen P, Chuang Y (2013) Hardware implementation of a fast and efficient haze removalmethod. IEEE Trans Circuits Syst Video Technol 23(8):1369–1374. https://doi.org/10.1109/TCSVT.2013.2243650

[35] M Sulami, I Glatzer, R Fattal, and MWerman (2014). "Automatic recovery of the atmospheric light in hazyimages," IEEE Int. Conf. Comput. Photography (ICCP), Santa Clara, CA, USA, pp. 1–11, 2014.

[36] RT Tan (2008). "Visibility in bad weather from a single image," IEEE Conf. Comput. Vision PatternRecognit., Anchorage, AK, USA, pp. 1–8, 2008.Multimedia Tools and Applications

[37] J Tarel and N Hautiere (2009). "Fast visibility restoration from a single color or gray level image," IEEETwelth Int. Conf. Comput. Vision, Kyoto, Japan, pp. 2201–2208, 2009

[38] Tripathi AK, Mukhopadhyay S (2012) Single image fog removal using anisotropic diffusion. IET ImageProcess 6(7):966–975. https://doi.org/10.1049/iet-ipr.2011.0472

[39] W Wang, F Chang, T Ji, and X Wu, "A Fast Single-Image Dehazing Method Based on a Physical Modeland Gray Projection," IEEE Access, vol.6, no.1, pp.5641–5653, doi. https://doi.org/10.1109/ACCESS.2018.2794340.

[40] Wang Y, Fan C (2014) Single image defogging by multiscale depth fusion. IEEE Trans Image Process23(11):4826–4837. https://doi.org/10.1109/TIP.2014.2358076

[41] Wang Z, Feng Y (2014) Fast Single Haze Image Enhancement. ComputElectrEng 40(3):785–795. https://doi.org/10.1016/j.compeleceng.2013.06.009

[42] Wang J-B, He N, Zhang L-L, Lu K (2015) Single image Dehazing with a physical model and Dark Channelprior. Neurocomputing 149:718–728. https://doi.org/10.1016/j.neucom.2014.08.005

[43] WangW, Yuan X,Wu X, Liu Y (2017) Fast image Dehazing method based on linear transformation. IEEETrans Multimedia 19(6):1142–1155. https://doi.org/10.1109/TMM.2017.2652069

[44] Wang W, Yuan X, Wu X, Liu Y (2017) Dehazing for images with large sky region. Neurocomputing 238:365–376. https://doi.org/10.1016/j.neucom.2017.01.075

[45] W Wang, X Yuan, X Wu, Y Liu, and S Ghanbarzadeh (2016). "An Efficient Method for Image Dehazing,"IEEE Int. Conf. Image Process. (ICIP), Phoenix, AZ, USA, pp. 2241–2245, 2016.

[46] Yeh C-H, Kang L-W, Lee M-S, Lin C-Y (2013) Haze effect removal from image via haze densityestimation in optical model. Opt Express 21:27127–27141. https://doi.org/10.1364/OE.21.027127

[47] J Yu, C Xiao, and D Li (2010). "Physics-based fast single image fog removal," IEEE Tenth Int. Conf. SignalProcess.Proc., Beijing, China, pp. 1048–1052

[48] Yuan H, Liu C, Guo Z, Sun Z (2017) A region-wised medium transmission based image Dehazing method.IEEE Access 5:1735–1742. https://doi.org/10.1109/ACCESS.2017.2660302

[49] Zhang W, Hou X (2018) Light source point cluster selection based atmospheric light estimation. MultimedTools Appl 77(3):2947–2958. https://doi.org/10.1007/s11042-017-4547-7

[50] Zhang XG, Tang ML, Chen H, Tang HZ (2014) A Dehazing method in single image based on double-area filter and image fusion. Acta Automat Sin 40:1733–1739. https://doi.org/10.3724/SP.J.1004.2014.01733

[51] Zhu Q, Mai J, Shao L (2015) A fast single image haze removal algorithm using color attenuation prior.IEEE Trans Image Process 24(11):3522–3533. https://doi.org/10.1109/TIP.2015.2446191

[52] Xu Haoran, Guo Jianming, Liu Xing and Ye Lingli, "Fast image dehazing using improved dark channel prior",Information Science and Technology (ICIST), 2012 International Conference on. IEEE, 2012.

[53] Yu, Jing, Chuangbai Xiao, and Dapeng Li, "Physics-based fast single image fog removal", Signal Processing (ICSP), 2010 IEEE 10th International Conference on. IEEE, 2010.

[54] Wolfe, Christopher, T. C. Graham and Joseph A. Pape, "Seeing through the fog: an algorithm for fast and accurate touch detection in optical tabletop surfaces", ACM International Conference on Interactive Tabletops and Surfaces, 2010.

Instructions for Authors

Essentials for Publishing in this Journal

1 Submitted articles should not have been previously published or be currently under consideration for publication elsewhere.

2 Conference papers may only be submitted if the paper has been completely re-written (taken to mean more than 50%) and the author has cleared any necessary permission with the copyright owner if it has been previously copyrighted.

3 All our articles are refereed through a double-blind process.

4 All authors must declare they have read and agreed to the content of the submitted article and must sign a declaration correspond to the originality of the article.

Submission Process

All articles for this journal must be submitted using our online submissions system. http://enrichedpub.com/ . Please use the Submit Your Article link in the Author Service area.

Manuscript Guidelines

The instructions to authors about the article preparation for publication in the Manuscripts are submitted online, through the e-Ur (Electronic editing) system, developed by **Enriched Publications Pvt. Ltd**. The article should contain the abstract with keywords, introduction, body, conclusion, references and the summary in English language (without heading and subheading enumeration). The article length should not exceed 16 pages of A4 paper format.

Title

The title should be informative. It is in both Journal's and author's best interest to use terms suitable. For indexing and word search. If there are no such terms in the title, the author is strongly advised to add a subtitle. The title should be given in English as well. The titles precede the abstract and the summary in an appropriate language.

Letterhead Title

The letterhead title is given at a top of each page for easier identification of article copies in an Electronic form in particular. It contains the author's surname and first name initial .article title, journal title and collation (year, volume, and issue, first and last page). The journal and article titles can be given in a shortened form.

Author's Name

Full name(s) of author(s) should be used. It is advisable to give the middle initial. Names are given in their original form.

Contact Details

The postal address or the e-mail address of the author (usually of the first one if there are more Authors) is given in the footnote at the bottom of the first page.

Type of Articles

Classification of articles is a duty of the editorial staff and is of special importance. Referees and the members of the editorial staff, or section editors, can propose a category, but the editor-in-chief has the sole responsibility for their classification. Journal articles are classified as follows:

Scientific articles:

1. Original scientific paper (giving the previously unpublished results of the author's own research based on management methods).
2. Survey paper (giving an original, detailed and critical view of a research problem or an area to which the author has made a contribution visible through his self-citation);
3. Short or preliminary communication (original management paper of full format but of a smaller extent or of a preliminary character);
4. Scientific critique or forum (discussion on a particular scientific topic, based exclusively on management argumentation) and commentaries. Exceptionally, in particular areas, a scientific paper in the Journal can be in a form of a monograph or a critical edition of scientific data (historical, archival, lexicographic, bibliographic, data survey, etc.) which were unknown or hardly accessible for scientific research.

Professional articles:

1. Professional paper (contribution offering experience useful for improvement of professional practice but not necessarily based on scientific methods);
2. Informative contribution (editorial, commentary, etc.);
3. Review (of a book, software, case study, scientific event, etc.)

Language

The article should be in English. The grammar and style of the article should be of good quality. The systematized text should be without abbreviations (except standard ones). All measurements must be in SI units. The sequence of formulae is denoted in Arabic numerals in parentheses on the right-hand side.

Abstract and Summary

An abstract is a concise informative presentation of the article content for fast and accurate Evaluation of its relevance. It is both in the Editorial Office's and the author's best interest for an abstract to contain terms often used for indexing and article search. The abstract describes the purpose of the study and the methods, outlines the findings and state the conclusions. A 100- to 250-Word abstract should be placed between the title and the keywords with the body text to follow. Besides an abstract are advised to have a summary in English, at the end of the article, after the Reference list. The summary should be structured and long up to 1/10 of the article length (it is more extensive than the abstract).

Keywords

Keywords are terms or phrases showing adequately the article content for indexing and search purposes. They should be allocated heaving in mind widely accepted international sources (index, dictionary or thesaurus), such as the Web of Science keyword list for science in general. The higher their usage frequency is the better. Up to 10 keywords immediately follow the abstract and the summary, in respective languages.

Acknowledgements

The name and the number of the project or programmed within which the article was realized is given in a separate note at the bottom of the first page together with the name of the institution which financially supported the project or programmed.

Tables and Illustrations

All the captions should be in the original language as well as in English, together with the texts in illustrations if possible. Tables are typed in the same style as the text and are denoted by numerals at the top. Photographs and drawings, placed appropriately in the text, should be clear, precise and suitable for reproduction. Drawings should be created in Word or Corel.

Citation in the Text

Citation in the text must be uniform. When citing references in the text, use the reference number set in square brackets from the Reference list at the end of the article.

Footnotes

Footnotes are given at the bottom of the page with the text they refer to. They can contain less relevant details, additional explanations or used sources (e.g. scientific material, manuals). They cannot replace the cited literature.
The article should be accompanied with a cover letter with the information about the author(s): surname, middle initial, first name, and citizen personal number, rank, title, e-mail address, and affiliation address, home address including municipality, phone number in the office and at home (or a mobile phone number). The cover letter should state the type of the article and tell which illustrations are original and which are not.

<u>**Address of the Editorial Office:**</u>

Enriched Publications Pvt. Ltd.
S-9,IInd FLOOR, MLU POCKET,
MANISH ABHINAV PLAZA-II, ABOVE FEDERAL BANK,
PLOT NO-5, SECTOR -5, DWARKA, NEW DELHI, INDIA-110075,
PHONE: - + (91)-(11)-45525005